Inhibition of the radioactive decay of the isomer ^{119m}Sn with the use of Mössbauer backscattering

S. K. Godovikov

Scientific-Research Institute of Nuclear Physics, M. V. Lomonosov Moscow State University, 119899 Moscow, Russia

(Submitted 8 September 1998)
Pis'ma Zh. Éksp. Teor. Fiz. **68**, No. 8, 599–603 (25 October 1998)

In research on the production of beams of coherent γ rays (γ-ray lasers), conditions under which a substantial change $\Delta\lambda/\lambda = -(0.114 \pm 0.027)$ in the radioactive decay constant λ (the isomeric level 89.53 keV ^{119m}Sn, $T_{1/2}=293$ days) can occur have been found experimentally for the first time. This is made possible by coherent Mössbauer (23.87 keV) backscattering from a resonant screen located nearby. An interpretation of the effect observed is proposed on the basis of the idea of dynamic synchronization of oscillations between a nuclear level and a standing wave of Mössbauer radiation. Possibilities for further increasing $\Delta\lambda/\lambda$ up to 0.5 are found. © *1998 American Institute of Physics.* [S0021-3640(98)00120-0]

PACS numbers: 23.90.+w, 23.20.Lv, 42.55.Vc, 33.45.+x, 29.30.Kv

Numerous attempts to produce beams of coherent γ rays (γ-ray lasers) have been made since the beginning of the 1960s, so far without success.[1] One of the most interesting variants of a γ-ray laser is considered to be a two-level scheme based on long-lived isomers such as ^{119m}Sn ($T_{1/2}=293$ days). In this case the excited isomeric state arises under prolonged neutron irradiation of the isotope ^{118}Sn in a reactor. In this way it is possible to obtain sources with very appreciable specific activity, controlling the decay of which is the subject of γ-ray laser physics. However, since the discovery of the laws of radioactive decay it has been known that the decay constant λ is an absolute constant, which for a given isotope does not depend on any external actions. Attempts to influence the decay rate by altering the chemical environment around an atom of the isotope, the pressure, temperature, and so on, gave at most $\Delta\lambda/\lambda \sim 10^{-4}-10^{-3}$. Individual record ($\sim 10^{-2}$) cases (^{235m}U, $E=76$ eV, $T_{1/2}=26$ min (Ref. 2) or ^{90m}Nb, $E=2.38$ keV, $T_{1/2}=19$ s (Ref. 3)) have been observed only for low-energy decays due to electron conversion, which strongly depend on the electronic structure of an atom of the isotope and of the surrounding matrix. At present there is no general theoretical approach to the problem of a large change in λ, just as there are no experimental solutions of the problem. In this connection, an attempt is made in the present work to influence the decay constant of the 89.53 keV level of ^{119m}Sn by using radiation from the intermediate 23.87 keV Mössbauer level.

Two ^{119m}Sn Mössbauer sources in the form of the chemical compound $CaSnO_3$ were

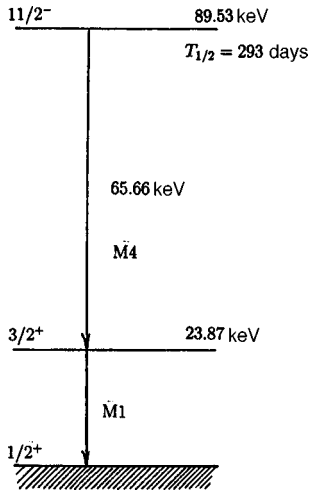

FIG. 1. Decay scheme of ^{119m}Sn.

used to perform the experiment. One source was subjected to a definite type of action, while the other was used as a reference standard. The activities of the sources at the start of the experimental series were 5 and 2 Ci, respectively. For the purposes of the present work, a ''black'' scatterer/screen, which has a Mössbauer effect probability $f'=1$ and contains a large quantity of the stable isotope, was produced by sintering a mixture of the powders CaO and $^{119}SnO_2$ in a definite proportion. The idea of the experiment is to place the ''black'' screen and source very close to one another (~ 2 mm) so that the γ wave emitted from the source and the wave from the resonant scatterer/screen could effectively interact with one another. The large solid angle ($\sim 2\pi$) of scattering into the source, the high probability of scattering, and coherence effects could provide the required effectiveness for influencing ^{119m}Sn nuclei which are in a ''predecay'' state. The decay scheme of ^{119m}Sn is shown in Fig. 1.[4] The isomeric level 89.53 keV is extremely strongly converted ($\alpha \sim 5000$) and lies far from the Mössbauer level 23.87 keV. It can be assumed that the nucleus, being a collective formation of nucleons where all energy levels are intercoupled and interdependent, will respond in one way or another to the proposed type of action.

The screen–source arrangement was left unchanged for six months. It was disturbed only once per month for ~ 1.5 h to perform measurements of the absolute intensity of the 23.8 keV line radiation. In so doing, the screen was removed and the source was secured in a strictly determined location in a spectrometric system. Measurements of the absolute intensity of a reference screen, which was not subjected to any influences, were made on the same day. The scintillation method of radiation detection and the multiscalar operating mode of the analyzer were used. For the first six months the experimental source (No. 1) was connected with the screen, after which the screen was removed and control measurements were performed on source No. 1 and the reference source No. 2 using the same scheme. The intensity of the reference source varies in time as $N_2 = N_{02}\exp(-\lambda t)$, while the intensity of the experimental source, where the decay constant is presumed to change ($\Delta\lambda$), varies as $N_1 = N_{01}\exp[-(\lambda+\Delta\lambda)t]$. Hence

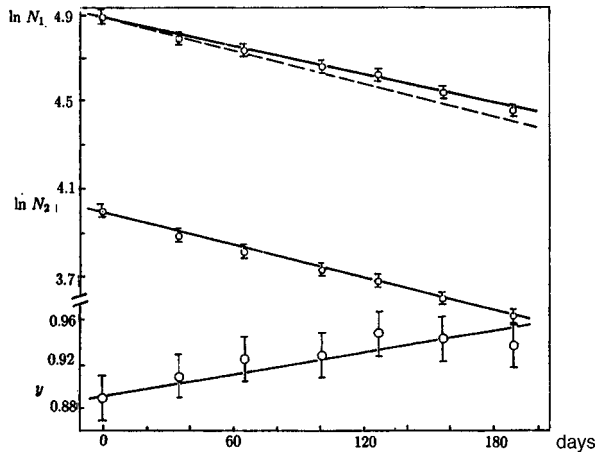

FIG. 2. Plots of $\log N_1$, $\log N_2$, and y versus time for an experiment with the screen in place, N is the counting rate per channel, $T=293$ K; the dashed line is parallel to $\log N_2$.

$$y=\log(N_1/N_2)=\log N_{01}-(\lambda+\Delta\lambda)t-\log N_{02}+\lambda t=(\log N_{01}-\log N_{02})-\Delta\lambda t. \qquad (1)$$

In the case $\Delta\lambda=0$ one will have $y=$ const, while for $\Delta\lambda\neq 0$ the plot of y is a straight line with slope $-\Delta\lambda$. The result of the measurements is a plot of y versus t.

The results of the analysis are presented in Fig. 2 (series with a screen) and Fig. 3 (control series). It is clear that in Fig. 2 the straight lines $\log N_1$ and $\log N_2$ as a function of t are not parallel, while the plot of y versus t is considerably different from $y=$const. At the same time, the straight lines $\log N_1$ and $\log N_2$ in Fig. 3 are completely parallel, and their difference corresponds to $y=$const.

The numerical results of the analysis are

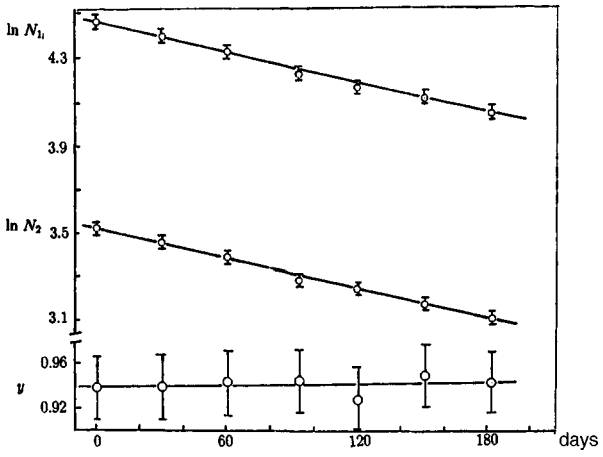

FIG. 3. Plots of $\log N_1$, $\log N_2$, and y versus time for the control experiment.

$\Delta\lambda = -(27 \pm 6) \times 10^{-5}$ day^{-1} for the experiment with a screen,

$\Delta\lambda = -(3 \pm 5) \times 10^{-5}$ day^{-1} for the control experiment.

The decay constant of the reference source, determined from the experimental data over a period of 12 months, is $\lambda = (236 \pm 3) \times 10^{-5}$ day^{-1}, i.e., $T_{1/2} = 293.6 \pm 3.7$ days, which corresponds to data in Fig. 1.

In summary, for the experimental source $\Delta\lambda/\lambda = -(0.114 \pm 0.027)$ and $T_{1/2} = 331.6 \pm 14.3$ days, i.e., the half-life increased by ~ 40 days. At the same time, it is obvious that $\Delta\lambda/\lambda = 0$ for the control series of experiments, which attests to a high reliability and stability of the apparatus employed.

Source No. 1 was also used to perform a Mössbauer experiment with the screen in place for the purpose of studying the influence of backscattering on the width of the 23.8 keV emission line. The linewidth remained unchanged to within 1.5%.

The value obtained for $\Delta\lambda/\lambda$ was found to be extremely large and negative, i.e., substantial inhibition of the decay of the isomeric level is observed. Let us examine the process of the interaction of the resonant source with the resonant screen. The screen is located 2 mm from the source, the lifetime of the 23.87 keV level is 1.85×10^{-8} s, and the γ radiation reaches the screen in $\sim 0.6 \times 10^{-11}$ s, i.e., a ^{119}Sn nucleus in the screen that absorbs a γ photon starts to re-emit with a delay of $\sim 1/3000$ of the temporal length of the wave train. As is well known, Mössbauer scattering possesses a clear-cut coherence property, i.e., the incident and scattered waves can interfere with one another.[5] As a result, a single forward wave and the corresponding backward wave (i.e., the wave scattered by 180°) form in the source a standing electromagnetic wave with lifetime $\sim 10^{-8}$ s. It can be estimated that a 5 Ci source is subjected to the action of $\sim 1.5 \times 10^{-6}$ standing waves in 1 s (taking account of the 2π solid angle and the conversion coefficient of the 23.87 keV level $\alpha = 5.5$).

The ^{119m}Sn nucleus in a predecay state with excitation energy 89.53 keV and the rest of the standing wave oscillating at a nucleus form a system of nonlinearly coupled oscillators whose energies are almost multiples of one another to within the accuracy of the measurements ($89.53/23.87 \sim 4$). Under such conditions dynamic synchronization of the frequencies and phases of the oscillations of these oscillators is entirely possible. This means that the isomeric level of the nucleus, the nucleus itself, and the standing wave form a new nuclear system whose parameters differ somewhat from those of the initial ^{119m}Sn nucleus. Specifically, ordering of the oscillations can increase the stability of the nuclear level, i.e., increase the lifetime of the level, as is observed. A mechanical analog of this phenomenon is provided by the synchronization of the oscillations of a pendulum clock suspended on a moving beam (the Huygens effect),[6] while a nuclear analog is provided by the recent discovery that the energies of several lower excited levels of a series of nuclei (from Ag to Ba including ^{119}Sn) are even multiples of the energy of the first, lowest level in a given nucleus (the nuclear Huygens effect).[7,8] There is also an optical analog of this phenomenon — mode locking in distributed systems, where waves with nearly commensurate (multiple) frequencies are phase-matched, for example, mode locking in lasers.[6] The initial commensurateness of the frequencies of our system and the enormous (with respect to the intranuclear time scale $\sim 10^{-23}$ s) lifetime of the standing

wave ($\sim 10^{-8}$ s) are favorable for adequate development of processes leading to the synchronization of oscillations of the ''nuclear level–standing wave'' type.

The total time during which the standing waves act on an undecayed nucleus in the source (synchronization time) is ~ 0.03 s per second, i.e., $\sim 3\%$. If this value is taken as being close to the experimental value $\Delta\lambda/\lambda \sim 11\%$, then the decay probability of a given nucleus can be considered to decrease sharply ($\Delta\lambda/\lambda \to -1$) during its interaction with the standing wave.

A number of predictions concerning the inhibition of decay can be made on the basis of the proposed interpretation. They include the following:

1) If the activity of the experimental source is increased by several factors of 10, then the synchronization time can increase by up to $\sim 100\%$. This will lead initially to a sharp decrease in the γ-ray flux, i.e., the activity of the source seemingly decreases sharply. As a result, the synchronization time will decrease and the γ-ray flux will increase back to the initial value. This process will repeat, i.e., periodic oscillations of the intensity will arise, and a ''pulsating'' radioactive source will be formed.

2) The half-life for ^{119m}Sn Mössbauer sources with high specific activity should be longer. This is because as a high-activity source decays, a large amount of the stable isotope ^{119}Sn accumulates in it and starts to function as an effective screen. This conclusion was checked experimentally. An initially ~ 50 mCi source made 10 years ago was used for this. At the time of the experiment it contained one radioactive ^{119m}Sn atom per ~ 4000 stable ^{119}Sn atoms. The measurements showed a sharp inhibition of decay and gave $\Delta\lambda/\lambda \sim 0.5$.

The absence of changes in the linewidth of the Mössbauer spectrum under the conditions of the experiment with the screen in place can be explained by the fact that the 23.87 keV radiation arises after the 89.53 keV level decays, the decay being most likely in the absence of a standing wave at the nucleus. At the same time, the fact that the linewidth does not change in the present experiment attests to the absence of effects such as radiation trapping and ''nuclear exciton'' formation.

I thank L. A. Rivlin and A. V. Davydov for a discussion of the results.

[1] V. I. Vysotskiĭ and R. N. Kuz'min, *Gamma Lasers*, Moscow State University Press, Moscow, 1989.
[2] O. V. Vorykhalov, E. A. Zaĭtsev, V. V. Kol'tsov, and A. A. Rimskiĭ-Korsakov, Izv. Akad. Nauk Rossii, Ser. Fiz. **56**, 30 (1992).
[3] *Hyperfine Interactions and Nuclear Radiation* [in Russian], Moscow State University Press, Moscow, 1985.
[4] V. G. Alpatov, A. A. Antipov, G. E. Bizina *et al.*, Izv. Akad. Nauk Rossii Ser. Fiz. **53**, 2052 (1989).
[5] V. A. Belyakov, Usp. Fiz. Nauk **115**, 553 (1975) [Sov. Phys. Usp. **18**, 267 (1975)].
[6] I. I. Blekhman, *Synchronization in Nature and Technology*, Nauka, Moscow, 1981.
[7] Yu. V. Sergeenkov, Izv. Akad. Nauk Rossii Ser. Fiz. **62**, 2 (1998).
[8] O. I. Sumbaev, Izv. Akad. Nauk Rossii, Ser. Fiz. **62**, 6 (1998).

Translated by M. E. Alferieff

Predictions for the forward cone in diffractive deep inelastic scattering

N. N. Nikolaev
IKP(Theorie), FZ Jülich, D-52425 Jülich, Germany;
L. D. Landau Institute of Theoretical Physics, Russian Academy of Sciences, 117940 Moscow, Russia

A. V. Pronyaev
Department of Physics, Virginia Polytechnic Institute and State University, Blacksburg, VA 24061, USA

B. G. Zakharov
L. D. Landau Institute of Theoretical Physics, Russian Academy of Sciences, 117940 Moscow, Russia

(Submitted 17 September 1998)
Pis'ma Zh. Éksp. Teor. Fiz. **68**, No. 8, 604–609 (25 October 1998)

We calculate the diffraction slope B_D for diffractive deep inelastic scattering. We find a counterintuitive rise of B_D in going from exclusive diffractive excitation of vector mesons to excitation of continuum states with $M^2 \sim Q^2$. For the small-mass continuum we predict a rapid variation of B_D with M^2 on a scale of m_V^2 and a sharp drop of B_D for a small-mass continuum above the vector meson excitation. © *1998 American Institute of Physics.* [S0021-3640(98)00220-5]

PACS numbers: 13.60.Hb

The diffraction slope is one of the principal observables which measure the impact-parameter structure of diffractive scattering. The commissioning of the leading proton spectrometer (LPS) of the ZEUS detector at HERA[1] gave a long-awaited access to the transverse momentum transfer Δ and the diffraction slope $B_D = -\partial \log\{d\sigma_D/d\Delta^2)\}/\partial\Delta^2$ in diffractive deep inelastic scattering (DIS) $ep \to e'p'X$. The special interest in the diffraction slope for diffractive DIS stems from the fact that besides the mass M of the excited state X there emerges a new large scale: the virtual photon's mass $\sqrt{Q^2}$. The principal issue is what B_D depends on: M^2, Q^2, the mass m_V of the ground-state vector meson in the corresponding flavor channel, and/or the diffractive scaling variable $\beta = Q^2/(Q^2 + M^2)$ (hereafter Q^2, x and $x_{\mathbf{IP}} = x/\beta$ are the standard diffractive DIS variables).

This is a highly nontrivial issue because at fixed β diffraction proceeds into the high-mass continuum states X with $M^2 = Q^2(1-\beta)/\beta \gg m_V^2$. Our experience with diffraction of hadrons and/or real photons can be summarized as follows. For any two-body diffractive scattering $ac \to bd$, an essentially model-independent decomposition holds, $B_D = \Delta B_{ab} + \Delta B_{cd} + \Delta B_{\rm int}$, where ΔB_{ij} comes from the size of the ij transition vertex and the relatively small $\Delta B_{\rm int}$ comes from the interaction range proper.[2,3] The values of ΔB_{ij} depend strongly on the excitation energy in the $i \to j$ transition, $\Delta M^2 = m_j^2 - m_i^2$. In

elastic scattering, $i=j$, one finds $\Delta B_{ii}\approx 1/3R_i^2\sim 4$–$6$ GeV^{-2}, where R_i^2 is the mean squared hadronic radius, and typically $B_{el}\sim 10$ GeV^{-2}. The similar estimate $\Delta B_{ij}\approx 1/3R_i^2, 1/3R_j^2$ holds for diffraction into low-mass continuum states, $\Delta M^2\lesssim m_N^2$, and diffraction into low-mass continuum and elastic scattering fall into the broad category of *exclusive* diffraction for which $B_D\sim B_{el}$. However, for excitation of high-mass continuum, $\Delta M^2\gtrsim m_N^2$, often referred to as the triple-pomeron (3**IP**) and/or genuine *inclusive* region of diffraction, the size of the diffracting particle no longer contributes to the diffraction slope and $B_D=B_{3\mathbf{IP}}=\Delta B_{pp}+\Delta B_{\rm int}\sim 1/2B_{el}\approx 6$ GeV^{-2}. The above slope $B_{3\mathbf{IP}}$ is nearly universal for all the diffracting beams and excited states X (Ref. 3). Furthermore, in the double high-mass diffraction $hp\to XY$, when $M_{X,Y}\gg m_N$, one is left with very small $B_D\sim\Delta B_{\rm int}\sim 1.5$–$2$ GeV^{-2} (see Refs. 2 and 4 and references cited therein). In real photoproduction the excitation scale is definitely set by the ground-state vector meson mass m_V. Perhaps the most dramatic example of this distinction between exclusive and inclusive diffraction is a drastic change of the diffraction slope from elastic, $pA\to pA$, to quasielastic, $pA\to p'A^*$, scattering of protons on heavy nuclei.[5]

Another well understood diffractive process is the elastic production of vector mesons $\gamma^*p\to p'V$. In this case the transverse size in the $\gamma^*\to V$ transition vertex, the so-called scanning radius

$$r_S=6/\sqrt{Q^2+m_V^2}, \tag{1}$$

decreases with Q^2 (and m_V^2). This is the basis for the prediction[6] that $\Delta B_{\gamma^*V}\propto r_S^2$ and that the diffraction slope B_V decreases to $B_V\approx B_{3\mathbf{IP}}$ at very large Q^2, which is in good agreement with the experiment.[7]

In this paper we report predictions for the Q^2, M^2 and flavor dependence of the diffraction slope for inclusive diffractive DIS. We demonstrate that in striking contrast to B_V for exclusive diffraction into vector mesons which exhibits strong dependence on Q^2, the diffraction slope B_D for inclusive diffractive DIS is a scaling function of β. The most paradoxical prediction is that in contrast to real photon and hadronic diffraction, in diffractive DIS B_D rises with the excited mass M reaching $B_D\sim B_{el}$ at $M^2\sim Q^2$. Arguably, such an unusual behavior of B_D derives from the scaling scanning radius r_S for diffraction excitation of continuum $q\bar{q}$ states,[8]

$$r_S^2\sim\frac{9}{m_f^2}(1-\beta), \tag{2}$$

which rises towards small β, so that $\Delta B_{\gamma^*X}\propto r_S^2$ does not depend on Q^2 and rises substantially from $\beta\approx 1$ to $\beta\sim 1/2$. Such a large, Q^2-independent ΔB_{γ^*X} has been conjectured earlier,[9] and in the present communication we quantify this property of the diffraction slope by a direct calculation. Furthermore, we predict a substantial drop of B_D below $B_{3\mathbf{IP}}$ for excitation of the small-mass continuum.

Finally, for very large excited masses, $M^2\gg Q^2$, i.e., $\beta\ll 1$, even for the $q\bar{q}$ excitation one recovers the inclusive regime of small ΔB_{γ^*X} and B_D decreases back to $B_D\sim B_{3\mathbf{IP}}$. This triple-pomeron limit of $\beta\ll 1$ is dominated by excitation of the $q\bar{q}g$ and higher Fock states of the photon, though, which is the genuinely inclusive process, and by the same token as for hadronic diffraction one can argue[9] that B_D must not depend on Q^2 and that $B_D\approx B_{3\mathbf{IP}}$. This expectation has been confirmed by the first data from the ZEUS

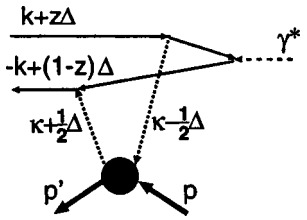

FIG. 1. One of the four Feynman diagrams for diffraction excitation of the $q\bar{q}$ final state via QCD two-gluon pomeron exchange.

LPS: $B_D=7.2\pm 1.1(\text{stat.})^{+07}_{-0.9}(\text{syst.})$ GeV^{-2} for diffractive DIS ($5<Q^2<20$ GeV^{-2}; Ref. 1) and $B_D=6.8\pm 0.9(\text{stat.})^{+1.2}_{-1.1}(\text{syst.})$ GeV^{-2} in real photoproduction ($Q^2=0$).[10]

We focus on diffractive excitation of the $q\bar{q}$ Fock states of the photon, which is known to dominate at $\beta\gtrsim 0.1$ (Ref. 11). The sample Feynman diagram for this process is shown in Fig. 1, in which we show also all the relevant momenta. We base our analysis on the formalism of Ref. 12, which we generalize to the non-forward case $\mathbf{\Delta}\neq 0$.[a)]

If z and $(1-z)$ are fractions of the (light-cone) momentum of the photon carried by the quark and antiquark, respectively and $\mathbf{k}$ is the relative transverse momentum in the $q\bar{q}$ pair, then $M^2=(m_f^2+k^2)/z(1-z)$. The quark and antiquark are produced with the transverse momenta $\mathbf{k}+z\mathbf{\Delta}$ and $-\mathbf{k}+(1-z)\mathbf{\Delta}$ with respect to the $\gamma^* p$ collision axis. We focus on the transverse diffractive structure function. To the leading $\log 1/x_{\mathbf{IP}}$, for excitation of quarks of mass m_f and electric charge e_f,

$$F_T^{D(4)}(\mathbf{\Delta}^2,x_{\mathbf{IP}},\beta,Q^2)=\frac{8\pi e_f^2}{3\sigma_{\rm tot}(pp)}\int\frac{d^2\mathbf{k}}{2\pi}\frac{(k^2+m_f^2)\beta}{(1-\beta)^2 J}$$
$$\times\alpha_S^2(\bar{Q}^2)\{[1-2z(1-z)]\mathbf{\Phi}_1^2+m_f^2\Phi_2^2\}, \tag{3}$$

where $J=\sqrt{1-4(k^2+m_f^2)/M^2}$, $\alpha_S^2(\bar{Q}^2)$ is the strong coupling, evaluated at the QCD hardness scale $\bar{Q}^2$ to be specified below, and $f(x_{\mathbf{IP}},\boldsymbol{\kappa},\mathbf{\Delta})$ is the gluon density matrix.[6,15] In the calculation of diffractive helicity amplitudes $\mathbf{\Phi}_1,\Phi_2$ it is convenient to introduce

$$\psi(z,\mathbf{k})=\frac{1}{\mathbf{k}^2+m_q^2+z(1-z)Q^2},\quad \mathbf{\Psi}(z,k)=\mathbf{k}\psi(z,\mathbf{k}), \tag{4}$$

in terms of which

$$\Phi_i=\int\frac{d^2\boldsymbol{\kappa}}{2\pi\boldsymbol{\kappa}^4}f(x_{\mathbf{IP}},\boldsymbol{\kappa},\mathbf{\Delta}_\perp)\,\phi_i, \tag{5}$$

where

$$\boldsymbol{\phi}_1=\mathbf{\Psi}(z,\mathbf{r}+\boldsymbol{\kappa})+\mathbf{\Psi}(z,\mathbf{r}-\boldsymbol{\kappa})-\mathbf{\Psi}\left(z,\mathbf{r}+\frac{1}{2}\mathbf{\Delta}\right)-\mathbf{\Psi}\left(z,\mathbf{r}-\frac{1}{2}\mathbf{\Delta}\right), \tag{6}$$

$$\phi_2=\psi(z,\mathbf{r}+\boldsymbol{\kappa})+\psi(z,\mathbf{r}-\boldsymbol{\kappa})-\psi\left(z,\mathbf{r}+\frac{1}{2}\mathbf{\Delta}\right)-\psi\left(z,\mathbf{r}-\frac{1}{2}\mathbf{\Delta}\right), \tag{7}$$

$$\mathbf{r}=\mathbf{k}-\frac{1}{2}(1-2z)\mathbf{\Delta}. \tag{8}$$

For small $\mathbf{\Delta}$ within the diffraction cone

$$\mathcal{F}(x,\boldsymbol{\kappa},\mathbf{\Delta})=\frac{\partial G(x,\kappa^2)}{\partial \log \kappa^2}\exp\left(-\frac{1}{2}B_{3\mathbf{IP}}\mathbf{\Delta}^2\right), \tag{9}$$

where $\partial G/\partial \log \kappa^2$ is the conventional unintegrated gluon structure function.[6] The dependence of $\mathcal{F}(x,\boldsymbol{\kappa},\mathbf{\Delta})$ on $\mathbf{\Delta}\boldsymbol{\kappa}$ corresponds to the subleading BFKL singularities[15] and can be neglected at small $x_{\mathbf{IP}}$. The diffraction slope $B_{3\mathbf{IP}}$ in (9) is a nonperturbative quantity, it comes for the most part form the hadronic size of the proton, modulo to a slow Regge growth one can take $B_{3\mathbf{IP}}\sim$ 6 GeV^{-2} (Ref. 6).

In the present analysis we are mostly concerned with the β,Q^2 and flavor dependence of $\Delta B_{\gamma^* X}$ which comes from the $\mathbf{\Delta}$ dependence of $\boldsymbol{\phi}_1$ and ϕ_2, and for our purposes it is sufficient to evaluate $\mathbf{\Phi}_1^2,\Phi_2^2$ to an accuracy $\mathbf{\Delta}^2$. The calculation of amplitudes $\mathbf{\Phi}_1,\Phi_2$ has been discussed to great detail in Refs. 8,12, and 16 and need not be repeated here. We simply cite the results starting with excitation of heavy quark–antiquark pair, when the fully perturbative quantum chromodynamics (pQCD) analytic calculation is possible:

$$F_T^{D(4)}(t,x_{\mathbf{IP}},\beta,Q^2)=\frac{2\pi e_f^2}{9\sigma_{\rm tot}(pp)}\frac{\beta(1-\beta)^2}{m_f^2}\Bigg[(3+4\beta+8\beta^2)+\frac{\Delta^2}{m_f^2}\frac{1}{10}(5-16\beta-7\beta^2 -78\beta^3+126\beta^4)\Bigg][\alpha_s(\overline{Q}^2)G(x_{\mathbf{IP}},\overline{Q}^2)]^2\exp(-B_{\mathbf{IP}}\mathbf{\Delta}^2), \tag{10}$$

where the pQCD hardness scale equals

$$\overline{Q}^2\approx m_f^2\left(1+\frac{Q^2}{M^2}\right)=\frac{m_f^2}{1-\beta}. \tag{11}$$

The result (10) holds for the large-mass continuum, $M^2\gg 4m_f^2$. As has been shown in Ref. 8, the typical transverse size in the $\gamma^*\to q\overline{q}$ transition vertex is $1/\overline{Q}$ (see Eq. (2)). For excitation of heavy flavors and/or for light flavors at $1-\beta\ll 1$ the hardness scale $\overline{Q}^2$ is large, and one is in the legitimate pQCD domain.

Consequently, the contribution to the diffraction slope from the γ^*X excitation vertex equals

$$\Delta B_{\gamma^* X}=\frac{1}{m_f^2}\frac{16\beta+7\beta^2+78\beta^3-126\beta^4-5}{10(3+4\beta+8\beta^2)}, \tag{12}$$

which is a rigorous pQCD result for heavy flavors. Evidently, it is a scaling function of β which does not depend on Q^2, a fact which nicely correlates with the scanning radius being a function of β only. It rises in going from $\beta\sim 1$ to $\beta\sim 1/2$ and decreases in the inclusive limit of $\beta\to 0$. It diminishes the diffraction slope at $\beta\sim 1$, which can be attributed to the *s*-channel helicity-nonconserving spin-flip transitions.

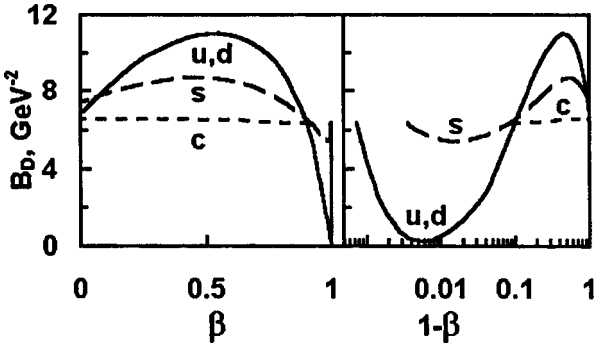

FIG. 2. Our predictions for the β and flavor dependence of the diffraction slope B_D in diffractive DIS of transverse photons at $Q^2=100$ GeV^2.

One can readily evaluate $\Delta B_{\gamma^* X}$ for the two terms $\propto \mathbf{\Phi}_1^2$ and $m_f^2\Phi_2^2$; we only mention here that for both terms the β dependence of $\Delta B_{\gamma^* X}$ is very similar to that given by Eq. (12). Even for heavy flavors, the contribution to $F_T^{D(4)}$ from $m_f^2\Phi_2^2$ is a numerically small correction to the dominant contribution from the term $\propto \mathbf{\Phi}_1^2$. This correction is even smaller for lighter flavors. As has been discussed in Ref. 16, the scale μ_G of variation of the unintegrated gluon density in the soft-to-hard transition region becomes more important than the mass m_f of light quarks. For this reason, for light flavor excitation the contribution from $m_f^2\Phi_2^2$ will be suppressed $\propto m_f^2/\mu_G^2$. Furthermore, the scale for $\Delta B_{\gamma^* X}$ will be set by $1/\mu_G^2$ rather than by $1/m_f^2$. One of the consequences is that the change of $\Delta B_{\gamma^* X}$ from strange to up/down quarks is much weaker than $\propto 1/m_f^2$ (see Fig. 2, where we show our numerical results).

Although for light flavor the magnitude of $\Delta B_{\gamma^* X}$ is no longer pQCD calculable, the behavior of the unintegrated gluon density in the soft-to-hard transition region is reasonably well tested from earlier calculations[16] of the diffractive structure function $F_T^{D(4)}$, which agree with experiment, and also from the small-Q^2 behavior of the proton structure function.[17] The emergence of this second scale has only a marginal impact on the β dependence of B_D, which is what we are concerned with here. We checked that variations of B_D calculated using different soft-to-hard interpolations of the gluon structure function as described in Ref. 16 do not exceed ~ 1 GeV^{-2}, with retention of the form of the β dependence of B_D.

In contrast to the scaling β dependence of B_D for finite β, for diffractive DIS into near-threshold small masses, $M^2 \sim m_V^2 \sim 4m_f^2$, i.e., for $1-\beta \propto M^2/Q^2 \ll 1$, we predict a strong M^2 dependence of the diffraction slope. The near-threshold region belongs to the pQCD domain even for light flavor excitation, because here the QCD hardness scale is large, $\overline{Q^2} \approx 1/4(Q^2+m_V^2)$ (for finite Q^2 and/or heavy flavor one must bear in mind the kinematical threshold $\beta \leqslant \beta_{\rm th}=Q^2/(Q^2+4m_f^2)<1$). The plane wave description of final states holds for quark–antiquark relative velocities $v \gtrsim \alpha_S(\overline{Q^2})$. In this case the small-v^2 expansion of diffractive structure function is

$$F_T^{D(4)}(t,x_{\mathbf{IP}},v,Q^2)=\frac{128\pi e_f^2}{3\sigma_{\rm tot}(pp)}\,\frac{m_f^2}{Q^4}v\left[1+\frac{\Delta^2}{6m_f^2}v^2\right]\left[\alpha_s(\overline{Q^2})G(x_{\mathbf{IP}},\overline{Q^2})\right]^2 \times \exp(-B_{\mathbf{IP}}\mathbf{\Delta}^2). \tag{13}$$

The principal effect is that the diffraction slope *decreases* with the increase of v^2 and/or M^2:

$$\Delta B_{\gamma^* X} = -v^2/6m_f^2. \tag{14}$$

Here for heavy flavors $v^2 = 1 - 4m_f^2/M^2$, while for light flavors it only makes sense to speak of the continuum above the ground-state $1S$ vector mesons (ρ^0, ω, ϕ^0), and v^2 must be understood as $v^2 \sim 1 - m_V^2/M^2$. Consequently, for the small-mass continuum we predict very rapid variations of the diffraction slope B_D (see Fig. 2), and here the relevant mass scale is m_V^2. The principal point is that B_D drops substantially; we leave open the scenario in which B_D becomes negative-valued, i.e., there will be a forward dip, in a certain range of masses.

In the spirit of duality for diffractive DIS,[18] diffraction excitation of the small-mass continuum above the $1S$ ground state vector meson is dual to production of radial excitations of vector mesons. Then our finding of the near-threshold decrease of the diffraction slope with rising M^2 correlates nicely with the prediction, which follows from the node effect,[6] that the diffraction slope is substantially smaller for the $V'(2S)$ states than for the ground state vector mesons $V(1S)$. The near-threshold drop of B_D is smaller for heavy flavors, in a nice conformity with the weaker node effect in diffractive production of heavy quarkonia.

A similar analysis can be repeated for the longitudinal diffractive structure function. Although it is of higher twist, it dominates diffractive DIS at $\beta \gtrsim 0.9$ (Refs. 18 and 16). As far as the diffraction slope is concerned, the QCD hardness scale for diffraction excitation of longitudinal photons is large, $\overline{Q}^2 \approx (1/4)\beta Q^2$, and the corresponding scanning radius is small, and we expect $B_D \approx B_{3\mathbf{IP}}$.

We conclude with a somewhat academic observation on a sum rule for the M^2 integrated cross section of diffractive excitation of heavy $q\bar{q}$ pairs by transverse photons. Namely, if one neglects the β dependence of the QCD hardness scale $\overline{Q}^2$ in (10), then one readily finds that for the M^2-integrated diffractive cross section $\Delta B_{\gamma^* X} = 0$ and $B_D = B_{3\mathbf{IP}}$. Indeed, a closer inspection of the calculation of the M^2 integrated cross section shows that to accuracy Δ^2 the dependence on $\mathbf{\Delta}$ can be eliminated by the change of integration variable $d^2\mathbf{k} \to d^2\mathbf{r}$. One can trace the origin of this sum rule to the QCD gauge-invariance properties of (5); it serves as a useful cross check of corresponding polynomial coefficients. This sum rule is of little practical value, though, because for the dominant excitation of light flavors the scale $\overline{Q}^2$ is small in the soft-to-hard transition region of strong variation of the gluon structure function $G(x_{\mathbf{IP}}, \overline{Q}^2)$, and the above-outlined derivation is not applicable.

To summarize, we have presented predictions from the standard two-gluon pomeron exchange mechanism for the forward cone in diffractive DIS. For the high-mass continuum excitation we predict that the diffraction slope B_D is a scaling function of β which has a counterintuitive rise in going from small masses to $M^2 \sim Q^2$, an effect which has no analog in the diffraction of real photons and/or hadrons. For the small-mass continuum we predict a rapid variation of B_D with M^2 on a scale of m_V^2 and a sharp drop of B_D for a small-mass continuum above the vector meson excitation. These predictions can be tested at HERA.

The work of B. G. Z. has been supported partly by INTAS Grant #96-0597 and the work of A. V. P. was supported partly by US DOE Grant #DE-FG02-96ER40994.

[a)]The first calculation of the diffraction slope for the M^2 integrated cross section is found in Ref. 13; the preliminary results from the present study have been reported elsewhere.[14]

[1] ZEUS Collaboration (J. Breitweg, M. Derrick, D. Krakauer *et al.*), Eur. Phys. J. **C1**, 109 (1998).
[2] H. Holtmann, N. N. Nikolaev, J. Speth *et al.*, Z. Phys. C **69**, 297 (1996).
[3] G. Alberi and G. Goggi, Phys. Rep. **74**, 1 (1981); T. J. Chapin, R. L. Cool, K. Goulianos *et al.*, Phys. Rev. D **31**, 17 (1985).
[4] C. Conta, M. Fraternali, F. Gigli-Berzolari *et al.*, Nucl. Phys. B **175**, 97 (1980).
[5] R. J. Glauber and G. Matthiae, Nucl. Phys. B **21**, 135 (1970).
[6] J. Nemchik, N. N. Nikolaev, E. Predazzi *et al.*, Zh. Éksp. Teor. Fiz. **113**, 1930 (1998) [JETP **86**, 1054 (1998)]; J. Nemchik, N. N. Nikolaev, E. Predazzi and B. G. Zakharov, Z. Phys. C **75**, 71 (1997); N. N. Nikolaev, B. G. Zakharov, and V. R. Zoller, Phys. Lett. B **366**, 337 (1996).
[7] ZEUS Collaboration (J. Breitweg, S. Chekanov, M. Derrick *et al.*), DESY-98-107; http://xxx.lanl.gov/abs/hep-ex/9808020.
[8] M. Genovese, N. Nikolaev, and B. Zakharov, Phys. Lett. B **378**, 347 (1996).
[9] N. N. Nikolaev and B. G. Zakharov, Zh. Éksp. Teor. Fiz. **105**, 1117 (1994) [JETP **78**, 598 (1994)]; Z. Phys. C **64**, 631 (1994).
[10] ZEUS Collaboration (J. Breitweg, M. Derrick, D. Krakauer *et al.*), Eur. Phys. J. C **2**, 237 (1998).
[11] M. Genovese, N. N. Nikolaev, and B. G. Zakharov, Zh. Éksp. Teor. Fiz. **108**, 1141 (1995) [JETP **81**, 625 (1995)].
[12] N. N. Nikolaev and B. G. Zakharov, Phys. Lett. B **332**, 177 (1994); Z. Phys. C **53**, 331 (1992).
[13] A. V. Pronyaev and B. G. Zakharov, unpublished; A. V. Pronyaev, Diploma Thesis, Moscow Institute for Physical Engineering (1992).
[14] N. N. Nikolaev and B. G. Zakharov, ''Phenomenology of diffractive DIS,'' in *Deep Inelastic Scattering and QCD (DIS97)*, Proceedings of the 5th International Workshop, Chicago, Ill., USA, April 14–18, 1997, AIP Conf. Proc. No.407, edited by J. Repond and D. Krakauer, p.445; A. Pronyaev, ''The forward cone and L/T separation in diffractive DIS,'' http://xxx.lanl.gov/abs/hep-ph/9808432, to be published, in *Proceedings of the 6th International Workshop on Deep Inelastic Scattering and QCD (DIS 98)*, Brussels, Belgium, April 4–8, 1998.
[15] L. N. Lipatov, Zh. Éksp. Teor. Fiz. **90**, 1536 (1986) [Sov. Phys. JETP **63**, 904 (1986)]; L. N. Lipatov, in *Perturbative Quantum Chromodynamics*, edited by A. H. Mueller, World Scientific (1989); E. A. Kuraev, L. N. Lipatov, and S. V. Fadin, Zh. Éksp. Teor. Fiz. **71**, 840 (1976) [Sov. Phys. JETP **44**, 443 (1976)]; Zh. Éksp. Teor. Fiz. **72**, 377 (1977) [Sov. Phys. JETP **45**, 199 (1977)].
[16] M. Bertini, M. Genovese, N. N. Nikolaev *et al.*, Phys. Lett. B **422**, 238 (1998).
[17] N. N. Nikolaev, B. G. Zakharov and V. R. Zoller, JETP Lett. **66**, 138 (1997); N. N. Nikolaev and B. G. Zakharov, Phys. Lett. B **327**, 157 (1994).
[18] M. Genovese, N. Nikolaev, and B. Zakharov, Phys. Lett. B **380**, 213 (1996).

Published in English in the original Russian journal. Edited by Steve Torstveit.

Spontaneous emission from an atomic oscillator located near an ideally conducting conical surface

V. V. Klimov[a)]
P. N. Lebedev Physics Institute, Russian Academy of Sciences, 117294 Moscow, Russia

(Submitted 17 September 1998)
Pis'ma Zh. Éksp. Teor. Fiz. **68**, No. 8, 610–613 (25 October 1998)

The linewidth for an atom located near an ideally conducting tip or inside a conical cavity in an ideal conductor is analyzed. It is shown that the effect of the tip decreases as its opening angle decreases. At the same time, the linewidth for an atom in a conical cavity can strongly increase or strongly decrease, depending on the position of the atom and the opening angle of the cavity. The results obtained could be helpful in designing spectrally-selective near-field nanoscopes. [S0021-3640(98)00320-X]

PACS numbers: 32.70.Jz, 61.16.Ch

A variety of works on the effect of material bodies on the spontaneous emission from an atom have now been published.[1,2] The effect of dielectric microspheres and cavities on the radiative lifetime of an atom is being discussed especially actively (see, for example, Refs. 3 and 4). At the same time, at present the main element of scanning microscopes is a nanotip, and there arises the question of the effect of this tip on the lifetime of an atom located near it. Numerical calculations of the effect of a conical tip with a complicated shape on the spontaneous emission were performed in Ref. 5. However, as far as I know, the problem of the linewidth for an atom in the presence of a conical tip or a conical cavity has not been widely discussed from the theoretical standpoint. The objective of the present letter is to examine this question. Although a systematic calculation of the linewidth requires a quantum-electrodynamic approach, we shall examine as a first approximation the radiation from a classical electric dipole whose electric moment d_0 and frequency are determined in the standard manner from quantum mechanics. It is well known that such an approach gives the correct results.[1,2]

As a first step, let us consider a radially oriented dipole lying on the axis of a cone. The geometry of the problem is shown in Fig. 1. In this case the electric field is known in all space:[6]

$$E_r=\frac{\partial^2 U}{\partial r^2}+k^2U; \quad E_\theta=\frac{1}{r}\frac{\partial^2 U}{\partial r\partial\theta}; \quad E_\varphi=\frac{1}{r\sin\theta}\frac{\partial^2 U}{\partial r\partial\varphi},$$

$$U=2id_0k\frac{r}{r_0}\sum_{n=1}^{\infty}P_{\nu_n}(\cos\theta)\frac{j_{\nu_n}(kr_0)h^{(1)}_{\nu_n}(kr)}{N_n}. \tag{1}$$

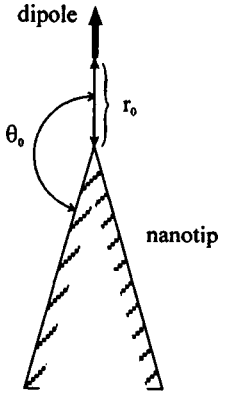

FIG. 1. Geometry of the problem of spontaneous emission from an atomic oscillator near a conical surface.

Here d_0 is the amplitude of the oscillations of the dipole moment; P_ν, j_ν, and $h_\nu^{(1)}$ are Legendre, spherical Bessel, and Hankel functions;[7] ν_n is the set of solutions of the equation $P_{\nu_n}(\cos\theta_0)=0$ that ensure satisfaction of the boundary condition; $k=\omega/c$ is the wave number in free space; and, the norm N_n is given by

$$N_n=\int_0^{\theta_0}\sin\theta d\theta(P_{\nu_n}(\cos\theta))^2=-\frac{\nu_n}{2\nu_n+1}P_{\nu_n-1}(\cos\theta_0)\frac{\partial P_{\nu_n}(\cos\theta_0)}{\partial\nu_n}. \qquad (2)$$

Figure 2 shows the behavior of several roots as a function of the opening angle of the cone. For not too small angles at the vertex ($\pi/6<\theta<5\pi/6$) the roots and norms can be estimated as

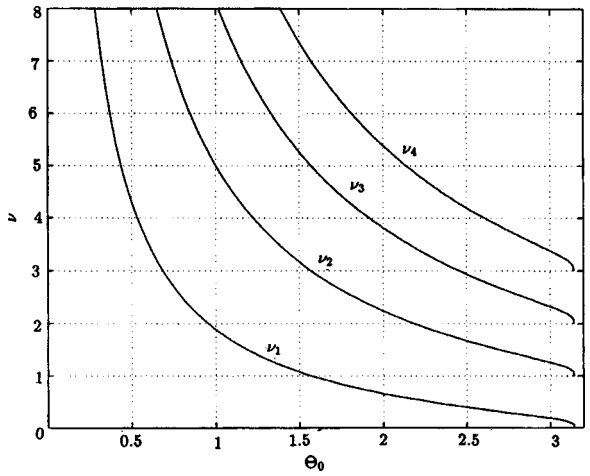

FIG. 2. Some roots of the equation $P_{\nu_n}(\cos\theta)=0$ ($n=1, 2, 3$) as a function of the opening angle of the conical surface.

$$\nu_n=\frac{\pi}{\theta}\left(n-\frac{1}{4}\right)-\frac{1}{2}+\frac{\cot\theta}{8\pi n}+O\left(\frac{1}{n^2}\right),\quad n=1,2,3..,\tag{3}$$

$$N_n=\frac{1}{2\nu_n+1}(3/2+1/\pi)\left(\frac{\Gamma(\nu_n+1)}{\Gamma(\nu_n+3/2)}\right)^2.$$

To calculate the linewidth we shall calculate the emitted energy flux in the wave zone. In this zone the field is transverse and it is sufficient to calculate only the θ component of the electric field, which assumes the form

$$E_\theta=-\frac{2d_0k}{r_0r}\sum_{n=1}^{\infty}\frac{\partial P_{\nu_n}(\cos\theta)}{\partial\theta}\frac{j_{\nu_n}(kr_0)}{N_n}\exp\{i(kr-(\nu_n+1)\pi/2)\}.\tag{4}$$

Substituting this expression into the Poynting vector and using the orthogonality relation

$$\int_0^{\theta_0}\frac{\partial P_{\nu_n}(\cos\theta)}{\partial\theta}\frac{\partial P_{\nu_{n'}}(\cos\theta)}{\partial\theta}\sin\theta d\theta=\delta_{nn'}\nu_n(\nu_n+1)N_n,\tag{5}$$

we obtain an expression for the total energy emitted per unit time:

$$\frac{dE}{dt}=\frac{ck^2d_0^2}{r_0^2}\sum_n\frac{\nu_n(\nu_n+1)}{N_n}j_{\nu_n}^2(kr_0).\tag{6}$$

Now, dividing this expression by the power of the radiation of the same dipole in free space,

$$\left(\frac{dE}{dt}\right)_0=\frac{cd_0^2}{3}k^4,\tag{7}$$

we obtain the final expression for the relative linewidth

$$\frac{\gamma}{\gamma_0}=\frac{3}{(kr_0)^2}\sum_n\frac{\nu_n(\nu_n+1)}{N_n}j_{\nu_n}^2(kr_0).\tag{8}$$

In the case $\theta_0=\pi/2$ the conical surface becomes flat, and the expression for the linewidth acquires the simpler form

$$\frac{\gamma}{\gamma_0}=\frac{3}{(kr_0)^2}\sum_{n=1}^{\infty}(2n-1)2n(4n-1)j_{2n-1}^2(kr_0).\tag{9}$$

Using the addition formula for Bessel functions[7]

$$\frac{\sin\lambda R}{\lambda R}=\sum_{n=0}(2n+1)j_n(\lambda r)j_n(\lambda\rho)P_n(\cos\theta),\tag{10}$$

$$R=\sqrt{r^2+\rho^2-2r\rho\cos\theta}$$

we can sum the series in Eq. (9), obtaining the expression

$$\frac{\gamma}{\gamma_0}=1-\frac{3\cos(2kr_0)}{(2kr_0)^2}+\frac{3\sin(2kr_0)}{(2kr_0)^3},\tag{11}$$

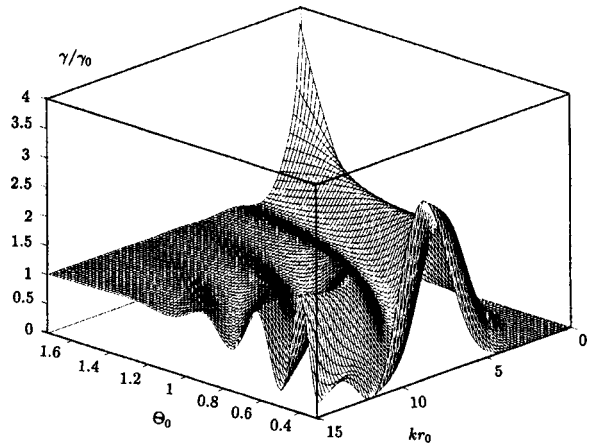

FIG. 3. Relative linewidth of a radially oriented dipole versus the position of the dipole on the axis and versus the opening angle of the conical surface.

which, of course, is identical to the expression for the linewidth in the presence of a conducting plane.[1]

For small distances from the vertex of the cone, $kr_0 \ll 1$, the first term plays the main role in expression (8), and

$$\frac{\gamma}{\gamma_0} \approx \frac{3\pi}{16} \frac{\nu_1(\nu_1+1)}{N_1 \Gamma^2(\nu_1+3/2)} \left(\frac{kr_0}{2}\right)^{2\nu_1-2}, \tag{12}$$

which, with the use of the approximate formula for the norm (3), becomes

$$\frac{\gamma}{\gamma_0} \approx \frac{3\pi^2}{8(3\pi+2)} \frac{\nu_1(\nu_1+1)(2\nu_1+1)}{\Gamma^2(\nu_1+1)} \left(\frac{kr_0}{2}\right)^{2(\nu_1-1)}, \tag{13}$$

$$\nu_1 = \frac{3\pi}{4\theta_0} - \frac{1}{2} + \frac{\cot\theta_0}{8\pi}.$$

In the case such that the distance of the atom from the tip is not small, Eq. (8) must be calculated numerically. The computational results are shown in Fig. 3. Analysis of this figure shows that a conical tip ($\theta_0 > \pi/2$) strongly influences the linewidth (broadening) only when the atom approaches the vertex. As the opening angle decreases ($\theta_0 \Rightarrow \pi$), the effect of the tip is seen only closer and closer to the vertex. This means that, actually, an infinitely sharp tip does not influence the spontaneous emission from an atom located at an arbitrarily close (but finite) distance from the tip.

A more interesting picture obtains when the atom lies inside a conical tip (inside a nanotip ($\theta_0 < \pi/2$)). In this case interference effects arise, and the linewidth depends strongly on the parameters of the problem. At some points it is considerably enlarged, while at other points it is considerably diminished. As the vertex is approached, the linewidth approaches zero, since radiation cannot escape from such a region at all.

The results obtained are easily extended to the case of an arbitrary orientation of the dipole. A more difficult problem is to calculating the frequency shift of an atomic oscillator in the presence of a conical surface and in taking nonideality of the reflecting surface into account. This problem will be examined in a separate publication.

I thank the Russian Fund for Fundamental Research for providing the financial support for this work.

[a)]e-mail: klimov@rim.phys.msu.su

[1]S. Haroche, in *Fundamental Systems in Quantum Optics*, Elsevier Science Publishers B. V., 1992.
[2]J. M. Wylie and J. E. Sipe, Phys. Rev. A **30**, 1185 (1984); **32**, 2030 (1985).
[3]V. V. Klimov, M. Ducloy, and V. S. Letokhov, J. Mod. Opt. **43**, 549 (1996).
[4]V. V. Klimov, M. Ducloy, and V. S. Letokhov, J. Mod. Opt. **43**, 2251 (1996).
[5]C. Girard, O. J. F. Martin, and A. Dereux, Phys. Rev. Lett. **75**, 3098 (1995).
[6]L. A. Vaĭnshteĭn, *Electromagnetic Waves* [in Russian], Radio i Svyaz', Moscow, 1988.
[7]M. Abramowitz and I. A. Stegan (Eds.), *Handbook of Mathematical Functions* (Dover, New York, 1965, Nauka, Moscow, 1979).

Translated by M. E. Alferieff

On resonance processes in near-threshold excitation of the resonance lines of a Zn^+ ion in electron–ion collisions

A. I. Imre, A. N. Gomonaĭ,[a)] V. S. Vukstich, and A. N. Nemet
Institute of Electronic Physics, Ukrainian National Academy of Sciences, 294016 Uzhgorod, Ukraine

(Submitted 22 September 1998)
Pis'ma Zh. Éksp. Teor. Fiz. **68**, No. 8, 614–617 (25 October 1998)

The excitation of the components of the $4p\,^2P^0_{1/2,3/2}$ resonance doublet of the Zn^+ ion by monoenergetic electrons in the interval 4–10 eV is investigated by a spectroscopic method in crossed beams. Resonances are found in the energy dependences below and above the excitation thresholds of resonance lines. The subthreshold resonances are satellite of the lines investigated and are excited in the process of dielectronic recombination. The main competing process here is the electronic decay of autoionizing states, which is manifested in a resonance excitation of the ions starting at the thresholds for the excitation of the levels. Autoionizing states lying between the levels of the doublet splitting of the $4p\,^2P^0_{1/2,3/2}$ state decay to the $4p\,^2P^0_{1/2}$ level in a Koster–Kronig process. Above the excitation energy of the $4p\,^2P^0_{3/2}$ level the the dominant contribution to resonance excitation is from autoionizing states with configurations $3d^9(^2D_{5/2,3/2})4s^2np,(n-1)f$. © *1998 American Institute of Physics.* [S0021-3640(98)00420-4]

PACS numbers: 34.80.Kw, 32.80.Dz

It is known that in the process of electron scattering by positively charged ions the attractive Coulomb field uncompensated by electrons produces characteristic features in the effective cross sections of processes occurring near the thresholds of new energetically closed channels. This is due to the formation and decay of autoionizing states (AISs) of the system ''electron + ion,'' i.e., to so-called resonance scattering. The formation of AISs is based on resonance capture of an incident electron with simultaneous excitation of the electron and the ion. They decay both by autoionization, with the emission of an electron, and radiatively, with emission of a photon. This specific feature of electron–ion interactions makes possible the formation of an excited system below the excitation thresholds of ionic levels. This is observed in the form of resonances in the elastic electron scattering cross sections of the ions or via dielectronic recombination (DR). At the thresholds, however, the more favorable electronic decay of AISs to excited levels of the ion becomes possible. This is observed as resonance excitation. As is shown in Ref. 1, it follows from detailed balance that in the absence of any external perturba-

tions the DR cross section (Q_{DR}) averaged over the resonances equals the excitation cross section of the corresponding core transition at the threshold (Q_{exc}), i.e.,

$$\lim_{n\to\infty} Q_{\mathrm{DR}}(n) = \lim_{k^2\to 0} Q_{\mathrm{exc}}(k^2, ij), \tag{1}$$

where i and j are the initial and final excited states of the ion. In the case of even weak perturbations due to an external electric field expression (1) breaks down, i.e., Q_{DR} can become much smaller than Q_{exc}.

On this basis it is of particular interest to make a direct experimental observation of resonances and to determine their role in near-threshold excitation of ions by electron impact. In the present letter we report the results of a spectroscopic investigation of resonances in the electron-impact excitation of the near-threshold parts of the individual components of the resonance doublet $4p\,^2P^0_{1/2,3/2}$ of the Zn^+ ion, and we propose a physical basis for the nature of the formation of these resonances.

In the experimental apparatus described in detail in Ref. 2, the electron and ion beams are crossed at a right angle under 5×10^{-8} torr vacuum conditions. The ion source operated in a low-voltage discharge regime. The discharge voltage ($U_r \leqslant 15$ V) was chosen to be absolutely less than the excitation energy of the lower of the long-lived $3d^9 4s^2\,^2D_{5/2,3/2}$ states of the Zn^+ ion. The energy of the ions was 600 eV and the ion current was $(6-8)\times10^{-7}$ A. A three-anode electron gun produced a ribbon electron beam in the energy range 4–10 eV, with a current of 5×10^{-5} Å and an energy width at half maximum of the electron energy distribution curve equal to $\Delta E_{1/2}=0.4$ eV. Spectral separation of the radiation was performed with a 70-degree vacuum monochromator, assembled in the Seya–Namioka scheme with a toroidal grating (radii 500 and 333 mm, 1200 lines/mm, Al coating). The inverse linear dispersion of the monochromator was $d\lambda/dl \sim 1.7$ nm/mm, and the spectral sensitivity in the wavelength range of the resonance lines of the Zn^+ ion ($\lambda=202.6$ and $\lambda=206.2$ nm) was $(5-8)\times10^{-5}$ counts/photon. A cooled FÉU-142 ''solar-blind'' photomultiplier was used as the radiation detector. The dark background of the photomultiplier was 1–2 counts/s.

The method of modulation of two beams by square voltage pulses phase-shifted by 1/4 of the modulation period was used to extract the signal due to the process under study from the total background (the background of the radiation detector and the background due to the collisions of electrons and ions with residual gas atoms). A signal of magnitude 1–5 counts/s was extracted from the background with signal/background ratio from 1/10 to 1/2. The process of performing the measurements and analyzing the results was automated using CAMAC modules and an IBM PC.

The results of a detailed investigation of the near-threshold sections (4–10 eV) of the energy dependences of the excitation of the resonance lines of the Zn^+ ion are presented in Figs. 1 and 2. The figures also show the energy positions and configurations of the AISs of the Zn atom from Ref. 3. The vertical bars on the experimental points show the rms errors in the relative measurements. The error in the absolute values of the effective cross sections does not exceed 15%. The electron energy scale was calibrated with an accuracy of ±0.05 eV from the threshold part of the excitation function of the resonance line of the Zn atom ($\lambda=213.9$ nm), for which the spectroscopic excitation threshold is known.

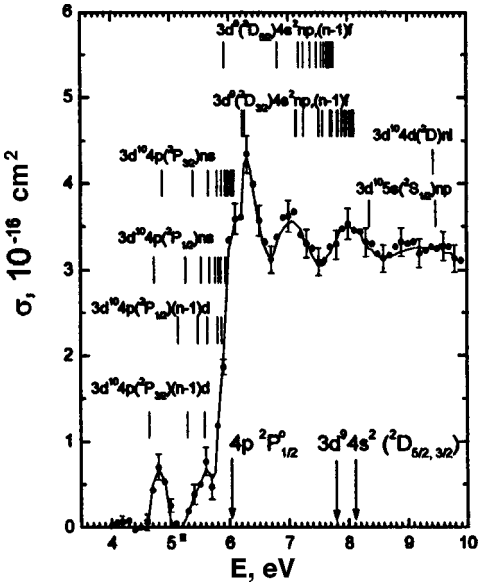

FIG. 1. Energy dependence of the effective electron-impact excitation cross sections of the dielectronic satellites $(3d^{10}4p(^2P^0_{1/2})ns,(n-1)d\rightarrow 3d^{10}4sns,(n-1)d^{1,3}L_j)$ and of the resonance line $\lambda=206.2$ nm $(4p\,^2P^0_{1/2}\rightarrow 4s\,^2S_{1/2})$ of the Zn^+ ion.

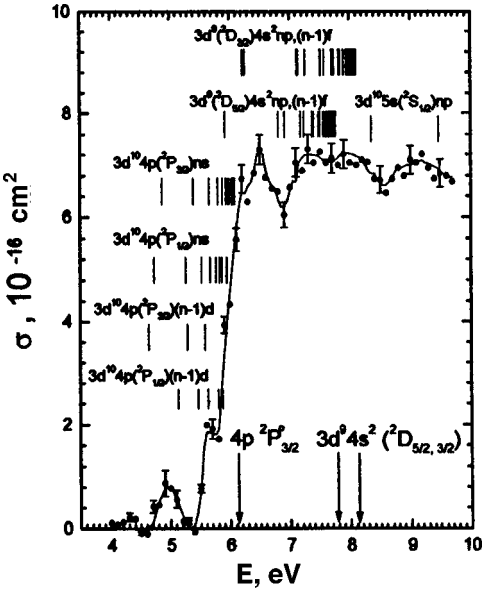

FIG. 2. Energy dependence of the effective electron-impact excitation cross sections of the dielectronic satellites $(3d^{10}4p(^2P^0_{3/2})ns,(n-1)d\rightarrow 3d^{10}4sns,(n-1)d^{1,3}L_j)$ and of the resonance line $\lambda=202.6$ nm $(4p\,^2P^0_{3/2}\rightarrow 4s\,^2S_{1/2})$ of the Zn^+ ion.

Distinct structure was observed in the energy dependences investigated, both below and above the excitation threshold of the resonance levels of the Zn^+ ion. This structure is due to resonance capture of incident electrons by Zn^+ ions, accompanied by excitation of the system to AISs of the Zn atom with configurations $3d^{10}4p(^2P^0_{1/2,3/2})ns$, $(n-1)d$ and $3d^9(^2D_{5/2,3/2})4s^2np,(n-1)f$ (where $n\geqslant 5$), followed by their decay in the electronic and radiation channels. Radiative stabilization of the AISs $3d^{10}4p(^2P^0_{1/2,3/2})ns,(n-1)d$ to the excited $3d^{10}4sns,(n-1)d^{1,3}L_j$ levels of the Zn atom is observed as dielectronic satellites of the resonance lines. Our approximate calculations showed that the dielectronic satellites of the resonance line $\lambda=206.2$ nm ($4^2P^0_{1/2}\rightarrow 4^2S_{1/2}$) are spectral lines emitted in the decay of AISs whose convergence limit is the $4p\,^2P^0_{1/2}$ level, while in the case of the resonance line $\lambda=202.6$ nm ($4^2P^0_{3/2}\rightarrow 4^2S_{1/2}$) the lines are associated with the decay of AISs that converge to the $4p\,^2P^0_{3/2}$ level. For clear separation of the components of the resonance doublet of the Zn^+ ion and for maximum transmission of the radiation of the satellite lines, the investigations were performed in the wavelength ranges $\lambda=206.2\pm 2$ nm and $\lambda=202.6\pm 2$ nm.

Analysis of the results shows that the individual resonance maxima in the curves at 4.8 eV in Fig. 1 and at 5.0 eV in Fig. 2 are most likely due to the decay of the $3d^{10}4p6s$ AISs to the $3d^{10}4s6s^{1,3}S$ levels of the Zn atom. For $n\geqslant 7$ the AISs with configurations $3d^{10}4p(^2P^0_{1/2,3/2})ns,(n-1)d$ are closely spaced in a narrow energy interval, so that the dielectronic satellites cannot be resolved spectroscopically and give a sum contribution to the DR process (see resonance maxima at energies 5.6 eV in Fig. 1 and 5.7 eV in Fig. 2). At energies close to the excitation thresholds of the resonance levels (6.01 eV and 6.12 eV), because of the energy width of the electrons, the DR process cannot be distinguished from the excitation of resonance lines in the experimental energy dependences.

For AISs with configurations $3d^{10}4p(^2P^0_{3/2})ns,(n-1)d$, located between the doublet levels of the $4p\,^2P^0_{1/2,3/2}$ resonance state of the Zn^+ ion, the dominant decay channel is electronic decay to the $4^2P^0_{1/2}$ level by the Koster–Kronig process

$$\mathrm{Zn}^{**}[3d^{10}4p(^2P^0_{3/2})ns,(n-1)d]\rightarrow \mathrm{Zn}^{+*}[3d^{10}4p(^2P^0_{1/2})]+\tilde{e}, \tag{2}$$

which results in additional resonance excitation of the $\lambda=206.2$ nm line at threshold. Since the doublet splitting ($\Delta E=0.11$ eV) is much smaller than the energy width of the electrons ($\Delta E_{1/2}=0.4$ eV), this resonance contribution is seen only as a kink in the excitation function (see Fig. 1).

In the energy interval from the excitation thresholds of the resonance lines up to the excitation energy of the first level from which cascade transitions to the resonance levels are possible (7.78 eV for $\lambda=202.6$ nm and 8.12 eV for $\lambda=206.2$ nm), the observed resonance features can be explained by the electronic decay of AISs with configurations $3d^9(^2D_{5/2,3/2})4s^2np,(n-1)f$. As one can see from Figs. 1 and 2, the sharpest peaks are the ones that coincide in energy with individual AISs. In the energy interval where the AISs are more closely spaced, their contribution is manifested in the curves in the form of wider peaks, which result from averaging over many resonances.

It should be noted that the contribution to the effective excitation cross sections of the resonance lines from resonance excitation via AISs with configurations $3d^9(^2D_{5/2,3/2})4s^2np,(n-1)f$ is greater than the contribution from that via AISs with

configurations $3d^{10}5s(^2S_{1/2})np$ and $3d^{10}4d(^2D)nl$, i.e., the excitation of the subvalent $3d^{10}$ shell plays a large, and sometimes governing, role in the excitation of the Zn^+ ion.

In summary, our results attest to a complicated mechanism of near-threshold electron-impact excitation of the resonance lines of the Zn^+ ion. The mechanism involves the efficient occurrence of resonance processes — dielectronic recombination and resonance excitation. Dielectronic recombination is the main mechanism of excitation of the satellite lines that fall within a narrow wavelength range near the resonance line. The intensity of the dielectronic satellites is determined by the probabilities of both electron capture and radiative decay of the corresponding AISs. The main competing decay here is the electronic decay of AISs to the ground or excited states of the ion. The latter is manifested in the resonance excitation of the ions. Relativistic and correlation effects strongly influence the ratio of the radiative and electronic decay probabilities of AISs, and these effects become increasingly important for heavy atomic systems.

The physical basis that we have proposed for the nature of the observed resonance processes is of a qualitative character. Detailed theoretical investigations must also be performed in order to gain a deeper understanding of the mechanisms of these processes and to determine their quantitative contribution to different electron–ion scattering processes.

This work was supported in part by the International Union INTAS (Grant No. 96-0447).

[a)]e-mail: IEP@IEP.UZHGOROD.UA

---

[1] A. K. Pradhan, Phys. Rev. A **30**, 2141 (1984).
[2] A. N. Gomonaĭ and A. I. Imre, Ukr. Fiz. Zh. **41**, 1032 (1996).
[3] J. Sugar and A. Musgrove, J. Phys. Chem. Ref. Data **24**, 1803 (1995).

Translated by M. E. Alferieff

Giant nonlinear optical activity in an aggregated silver nanocomposite

V. P. Drachev and S. V. Perminov
Institute of Semiconductor Physics, Siberian Branch of the Russian Academy of Sciences, 630090 Novosibirsk, Russia

S. G. Rautian and V. P. Safonov
Institute of Automation and Electrometry, Siberian Branch of the Russian Academy of Sciences, 630090 Novosibirsk, Russia

(Submitted 26 August 1998)
Pis'ma Zh. Éksp. Teor. Fiz. **68**, No. 8, 618–622 (25 October 1998)

Nonlinear optical activity due to spatial dispersion is observed in a colloidal solution of silver. It is shown experimentally that the effect is substantially enhanced (by a factor of $\sim 10^2$) when the silver particles aggregate into fractal clusters. The self-rotation angle of the plane of polarization is 2 mrad at an intensity of 2 MW/cm^2 for $\lambda = 0.532$ μm and a pulse duration of 11 ns. A method of separating the contributions of the local and nonlocal effects to the rotation of the plane of polarization is proposed and implemented. © *1998 American Institute of Physics.* [S0021-3640(98)00520-9]

PACS numbers: 78.20.Ek, 42.65.An, 61.43.Hv

Nonlinear optical effects due to a substantial enhancement of the local electric field of a light wave in metallic nanocomposites have been under intensive investigation in the last few years (see reviews[1,2]). An example of such effects is the giant enhancement (by a factor of 10^6) of the conversion coefficient for four-photon scattering in the presence of aggregation of silver nanoparticles into fractal clusters.[3] The enhancement of the local field is due to the formation of collective modes of dipole excitation as a result of the interaction of dipoles induced by the light field in highly polarizable nanoparticles forming a disordered structure. The collective dipole modes can be realized on a small fraction of the elements of the structure. The size of the region of localization of the excitation depends on the morphology of the structure and the wavelength of the exciting light. In the case of fractal colloidal aggregates of silver, the size of the localization region (resonance domain) varies with wavelength and ranges from ~ 100 nm in the blue region of the spectrum down to ~ 20 nm in the near-IR region for ~ 10 nm particles.[4] Thus the ratio of the size of a particle (or group of particles forming a domain that effectively interacts with the light) to the wavelength is much greater than for ordinary molecular media. This circumstance is favorable for observing effects due to spatial dispersion in nonlinear optical processes in metallic nanocomposites. For nonlocal effects an important role is played not only by the enhancement of the local field but also by the increase in its gradient.

Nonlinear polarization phenomena in isotropic media have been studied in Refs. 5–7. Nonlinear rotation of the plane of polarization as a result of local and nonlocal third-order interactions has been observed in cubic crystals.[6]

In the present work we observed experimentally the nonlinear gyrotropy of fractal Ag clusters, which arises as a result of the nonlocal nature of the interaction, and enhancement of the gyrotropy upon aggregation of the silver nanoparticles in a colloidal solution. It is shown that for the second harmonic of YAG:Nd laser radiation with pulse duration $\tau=11$ ns the nonlinear rotation constant is large: 1.3×10^{-2} rad·cm/MW. A method was developed to separate the local and nonlocal nonlinear effects.

The nonlinear effects of spatial dispersion can be taken into account in the expression for the polarization of the medium by means of a term with the tensor $\hat{\Gamma}^{(3)}$:

$$P_i^{(3)}=\chi_{ijkl}^{(3)}E_jE_kE_l+\Gamma_{ijklm}^{(3)}E_jE_k\nabla_mE_l. \tag{1}$$

In an isotropic medium $\hat{\Gamma}^{(3)}$ has one nonzero component g_1. The local nonlinear response of an isotropic medium is described by two constants, χ_1 and χ_2, which are related with the cubic susceptibility tensor $\hat{\chi}^{(3)}$ as

$$\chi_1+\chi_2=\chi_{iiii}^{(3)},\quad \chi_{ijij}^{(3)}=\chi_{ijji}^{(3)}=\chi_1/2,\quad \chi_2=\chi_{iijj}^{(3)},\quad i,j=1,2;\quad i\neq j. \tag{2}$$

According to Ref. 8, the rotation angle $\alpha(z)$ of the polarization ellipse (the z axis is directed along the wave vector) is described by the equation

$$d\alpha/dz=\rho_0'+\rho_1'(|A_+|^2+|A_-|^2)+\sigma_2'(|A_+|^2-|A_-|^2), \tag{3}$$

where A_+ and A_- are the amplitudes of the circular components of the wave, $A_\pm=(A_x\pm iA_y)/\sqrt{2}$, $\rho_0=\rho_0'+i\rho_0''$ is the linear gyration constant, $\rho_1=2\pi g_1\omega^2/c^2=\rho_1'+i\rho_1''$, $\sigma_{1,2}=2\pi\omega^2\chi_{1,2}/kc^2=\sigma_{1,2}'+i\sigma_{1,2}''$, and $k=(\omega/c)(\mathrm{Re}\,\varepsilon_0)^{1/2}$. The first term corresponds to linear gyrotropy. We note immediately that this effect was not observed in our experiments, i.e., its contribution does not exceed 0.6 mrad/cm.

In a nongyrotropic medium ($\rho_0'=0$) the nonlinear rotation of the plane of polarization of a linearly polarized wave ($|A_+|^2=|A_-|^2$) is due solely to the nonlocal nature of the nonlinear response. In Eq. (3) the term containing the coefficient ρ_1' corresponds to this effect. In the case of elliptical polarization there is an additional rotation of the plane of polarization (the term containing σ_2').[9] Since under the conditions of the experiment the polarization of the radiation is always ''weakly elliptical,'' both terms must be taken into account. Our goal was to investigate the nonlocal rotation of the plane of polarization, and in this formulation the term with σ_2' serves as an instrumentational masking factor. For this reason, it was desirable to be able to separate the contributions coming from the indicated effects. In our experiments the following method was proposed and implemented. We note that $|A_+|^2-|A_-|^2=2|A_x||A_y|\sin(\phi_x-\phi_y)$, where $|A_{x,y}|$ and $\phi_{x,y}$ are the amplitudes and phases of the linearly polarized components of the field. By varying the phase difference $\phi_x-\phi_y$ it is possible to alter the contribution of the third term, while the contribution of the nonlocal response will remain constant.

The scheme of the polarization measurements is displayed in Fig. 1. Pulses of the second harmonic of the YAG:Nd laser were used. The pulse shape and the transverse distribution in the beam are also displayed in the same figure. The radiation passed successively through the polarizer *1* (a Glan prism), a phase element *3*, a cell *4* of

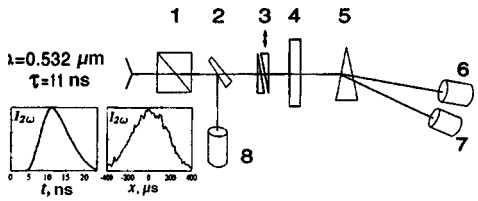

FIG. 1. Experimental arrangement.

thickness $l=3$ mm containing the experimental colloidal sample, and an analyzer *5* (a calcite wedge), and it was detected by two silicon photodiodes *6* and *7*. To measure the intensity a portion of the radiation was directed by the plate *2* onto the photodiode *8*. The radiation transmitted through the polarizer had a slight ellipticity with semiaxis ratio $|A_y|^2/|A_x|^2 \approx 5\times 10^{-5}$ (the x axis is directed along the axis of the polarizer and the y axis is directed perpendicular to it and to the wave vector). The phase element consisted of two identical wedges made of crystalline quartz cut so that its optic axis was directed along the y axis. Here the phase element acts as a phase plate of variable thickness. The components of the complex amplitude of the radiation transmitted through the phase element acquire an additional phase shift

$$A_x(0)=|A_x(0)|e^{i\phi_x(0)}, \quad A_y(0)=|A_y(0)|e^{i\phi_y(0)}, \quad \Delta\phi_0=\phi_x(0)-\phi_y(0). \tag{4}$$

The effect of the phase element is thus to change the azimuth and the ratio of the semiaxes of the polarization ellipse of the radiation at the entrance to the medium. The azimuth $\alpha(0)$ of the ellipse relative to the polarizer, with allowance for the smallness of the ratio $|A_y|/|A_x| \ll 1$, is given by the expression

$$\alpha(0)=\frac{|A_y(0)|}{|A_x(0)|}\cos(\Delta\phi_0). \tag{5}$$

The radiation transmitted through the experimental medium enters the analyzer, whose axis makes an angle of 45° with the polarizer. The orthogonally polarized components separated by the analyzer enter the photodiodes *6* and *7*. We recorded the difference of the signals from the photodiodes,

$$\Delta I=I_2-I_1\approx|A_x|^2 2\alpha, \tag{6}$$

where α is the azimuth of the polarization ellipse at the exit from the medium. Here we have made use of the fact that $\alpha \ll 1$ and also of the smallness of the ellipticity.

The functions $\Delta I(\Delta\phi_0)$ were measured in the experiment for different radiation intensities at the entrance to the medium. Let $\Delta\phi(z)=\Delta\phi_0+\Delta\phi_{NL}(z)$ and, since $\Delta\phi_{NL}(z)\ll 1$, we obtain from Eqs. (3)–(6)

$$\Delta I(\Delta\phi_0)=a+b\cos(\Delta\phi_0+c); \tag{7}$$

$$a=2\rho_1'|A_x(l)|^2\int_0^l|A_x|^2\,dz, \quad b=2|A_x(l)|^2\frac{|A_y(0)|}{|A_x(0)|}, \quad c=-2\sigma_2'\frac{|A_x(0)|}{|A_y(0)|}\int_0^l|A_x||A_y|\,dz.$$

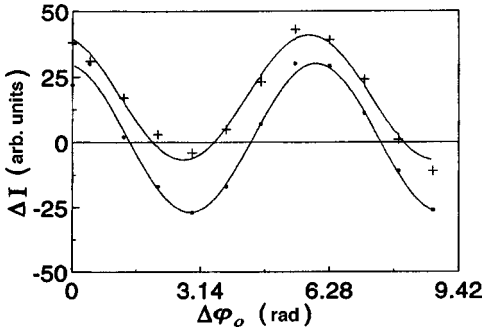

FIG. 2. Phase dependences $\Delta I(\Delta\phi_0)$ for different intensities I_0 at the entrance to the medium: □ — $I_0 = 0.3$ MW/cm^2; + — $I_0 = 2$ MW/cm^2.

Thus one can see that the local σ_2 and nonlocal ρ_1 nonlinearities are manifested differently in $\Delta I(\Delta\phi_0)$ as the intensity at the entrance varies: The term with σ_2' can lead to a phase shift, while the term with ρ_1' gives rise to a displacement of the curve $\Delta I(\Delta\phi_0)$ as a whole along the ordinate.

Figure 2 shows plots of the function $\Delta I(\Delta\phi_0)$, measured for two values of the radiation intensity. The values presented correspond to the peak (in time) intensity on the beam axis. As one can see, the functions are sinusoidal, to a high degree of accuracy, and an increase of the intensity also results in a vertical displacement of the entire curve as a whole and to a change in amplitude and a phase shift. The measured vertical displacement in the present case corresponds to an angle of nonlinear rotation of the plane of polarization $\alpha_g \approx 2 \pm 0.2$ mrad, whence $\rho_1' = \alpha_g / I_{\text{eff}} l \approx 1.3 \times 10^{-2}$ rad·cm/MW. Here $I_{\text{eff}} = (\int_0^l I(z)dz)/l$ is the effective value of the intensity in the cell, averaged over the pulse and cross section of the beam, taking into account the total (linear and nonlinear) absorption, which in our case are ≈ 2.3 cm^{-1} and ≈ -0.5 cm^{-1}, respectively. The rotation direction can be determined from the sign of the vertical displacement. A plus sign corresponds to counterclockwise rotation, looking into the beam.

The experiments were performed with an ethanol colloidal solution of silver stabilized with PVP (polyvinylpyrrolidone). The colloid was prepared by the method described in Ref. 10. The solutions contain isolated silver microparticles (monomers) about 10 nm in diameter. Aggregation was initiated by adding a small quantity of the alkali NaOH (5×10^{-5} parts by weight) to the solution. The degree of aggregation was monitored according to the characteristic broadening of the absorption spectrum of an aggregated colloid as compared with a nonaggregated colloid. Electron microscopy data[11] shows that samples with a long-wavelength wing in the spectrum consist of aggregates with $N \geqslant 1000$ monomers, while those without a wing do not contain large aggregates. Aggregates have a characteristic power-law relation between the number N of monomers and the radius R of the region which they occupy: $N \propto R^D$, where D is the fractal dimension. In our case $D \approx 1.7$. In the experiment we investigated the dependence of the nonlinear rotation angle on the intensity at the entrance for two colloids — strongly and weakly aggregated. The results are displayed in Fig. 3. The figure also shows (left inset) the nonlinear absorption spectra of the experimental samples. One can see that the nonlinear optical activity depends strongly on the degree of aggregation. Thus if the mea-

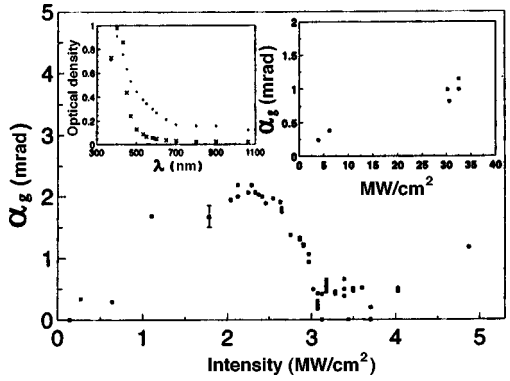

FIG. 3. Angle of nonlinear rotation of the plane of polarization versus the intensity at the entrance to the medium for strongly and weakly aggregated (right-hand inset) colloids. The silver particle density in the weakly aggregated colloid is approximately 2.4 times higher than in the strongly aggregated colloid. Left inset: Absorption spectra at low radiation intensity. □ — strongly aggregated colloid; + — weakly aggregated colloid.

surement data are scaled to the same silver density, then $\alpha_g/I_{\text{eff}} \propto \text{Re}\,\Gamma^{(3)}$ is approximately 80 times larger for a strongly aggregated colloid. It is noteworthy that the nonlinear constant decreases at intensities $I_0 > 2-3$ MW/cm^2 approximately corresponding to the threshold for photomodification of aggregates.[12] A similar manifestation of photomodification was observed in a previous work for the nonlinear refraction $\text{Re}\,\chi^{(3)}$ measured by dispersion interferometry.[13]

The tensor component $\Gamma^{(3)}$ can be found from the relation

$$\alpha_g = \frac{16\pi^4 l}{n_0 c \lambda^2} \times 10^{13} \text{Re}\,\Gamma^{(3)} I_{\text{eff}}\,[\text{MW/cm}^2], \tag{8}$$

where all quantities except the intensity are expressed in cgs esu and n_0 is the refractive index of the colloid. Taking into account the difference in the silver concentrations in the colloids and averaging over time and the beam cross section, which gives a factor of $2\sqrt{2}$, we obtain $\text{Re}\,\Gamma_s^{(3)} \approx 0.9 \times 10^{-16}$ cgs esu for a strongly aggregated colloid and $\text{Re}\,\Gamma_w^{(3)} \approx 1.1 \times 10^{-18}$ cgs esu for a weakly aggregated colloid. In both cases the medium is levorotatory. Let us compare the measured value of $\Gamma_s^{(3)}/\Gamma_w^{(3)}$ with an estimate based on the idea of aggregation-induced enhancement of the local field:

$$\Gamma_s^{(3)} = \Gamma_w^{(3)} F^2 N_r / N_m\,, \tag{9}$$

where $N_r/N_m \approx 0.3$ is the fraction of resonant monomers in a cluster, the enhancement factor of the local field is $F = (\varepsilon')^2/3n_0^2\varepsilon''$, and $\varepsilon = \varepsilon' + i\varepsilon''$ is the complex dielectric constant of silver. For $\lambda = 0.532$ μm, monomers of size ≈ 10 nm, $\varepsilon' \approx -10$, and $\varepsilon'' \approx 1$ we obtain $F \approx 18$, whence $\Gamma_s^{(3)} \approx 100\Gamma_w^{(3)}$, which agrees well with the measured value.

In summary, we have observed nonlinear gyrotropy in a colloidal solution of silver. The method proposed above made it possible to reliably distinguish the nonlinear gyrotropy. The nonlinear gyrotropy constant increases substantially with an increase in the degree of aggregation of the silver. Photoburnout of resonance domains in fractal aggre-

gates leads to a decrease in the rotation constant for $I(0)>2$ MW/cm^2. The cause of the nonlinear gyrotropy in silver nanocomposites consisting of spherically symmetric monomers and the sign of the nonlinear gyrotropy require further study.

This work was supported in part by the Russian Fund for Fundamental Research under Grants Nos. 96-02-19331 and 96-15-96642.

[1] V. M. Shalaev, Phys. Rep. **272**, 61 (1996).
[2] V. M. Shalaev, V. A. Markel, E. Y. Polyakov *et al.*, J. Nonlinear Opt. Phys. Mater. **7**, 131 (1998).
[3] S. G. Rautian, V. P. Safonov, P. A. Chubakov *et al.*, JETP Lett. **47**, 243 (1988).
[4] V. P. Safonov, V. M. Shalaev, V. A. Markel *et al.*, Phys. Rev. Lett. **80**, 1102 (1998).
[5] S. A. Akhmanov and V. I. Zharikov, JETP Lett. **6**, 137 (1967).
[6] S. A. Akhmanov, N. I. Zheludev, and R. S. Zadoyan, Zh. Éksp. Teor. Fiz. **91**, 984 (1986) [Sov. Phys. JETP **64**, 579 (1986)].
[7] S. V. Popov, Yu. P. Svirko, and N. I. Zheludev, J. Opt. Soc. Am. B **13**, 2729 (1996).
[8] S. A. Akhmanov, G. A. Lyakhov, V. A. Makarov, and V. I. Zharikov, Opt. Acta **29**, 1359 (1982).
[9] P. Maker, R. Terhune, and C. Savage, Phys. Rev. Lett. **12**, 507 (1964).
[10] H. Hirai and J. Macrom, Sci-Chem. A **13**, 633 (1979).
[11] Yu. E. Danilova and V. P. Safonov, in *Fractal Reviews in the Natural and Applied Sciences*, edited by M. M. Novak, Chapman and Hall, London, 1995, p. 101.
[12] A. V. Karpov, A. K. Popov, S. G. Rautian *et al.*, JETP Lett. **48**, 571 (1988).
[13] Yu. É. Danilova, V. P. Drachev, S. V. Perminov, and V. P. Safonov, Izv. Ross. Akad. Nauk, Ser. Fiz. **60**, 18 (1996).

Translated by M. E. Alferieff

Low-temperature specific heat of crystalline and amorphous $Eu_2(MoO_4)_3$

A. V. Pal'nichenko, E. G. Ponyatovskiĭ, B. S. Red'kin, and V. V. Sinitsyn[a)]
Institute of Solid-State Physics, Russian Academy of Sciences, 142432 Chernogolovka, Moscow Region, Russia

(Submitted 11 September 1998)
Pis'ma Zh. Éksp. Teor. Fiz. **68**, No. 8, 623–627 (25 October 1998)

The specific heat C_{total} of crystalline and amorphous $Eu_2(MoO_4)_3$ is measured in the temperature interval 4.5–30 K. The amorphous state is obtained by applying pressure ~ 7 GPa at room temperature. It is found that the specific heat of the crystal at $T \leqslant 7.5$ K is described by a cubic function of temperature, while the specific heat of the amorphous sample has a strongly non-Debye character in the entire experimental temperature interval. The curve of C_{total} for amorphous europium molybdate is analyzed in a model of soft atomic potentials, and it is shown that it agrees well with universal low-temperature anomalies of the specific heat of classical glasses obtained by quenching from the liquid.
 [S0021-3640(98)00620-3]

PACS numbers: 65.40.+g

The low-temperature behavior of glasses is a universal feature of the manifestation of disorder in condensed media.[1–4] Thus, at temperatures $T \leqslant 30-50$ K the temperature dependence of the specific heat and a number of other properties of various dielectric glasses (e.g., the thermal conductivity, sound velocity, etc.) differ considerably from those of crystalline solids, and in this sense they are anomalous. This difference is both quantitative (the specific heat of glasses at these temperatures is several times higher than that of the crystal analogs) and qualitative. The functional dependence of the specific heat for glasses is completely different from a dielectric crystal, which at low temperatures is described by the Debye law. Moreover, the character of the temperature dependence of the specific heat is insensitive to the chemical composition, the presence of impurities, and the past history of the glass. It can therefore be said that their low-temperature properties exhibit universality.

The anomalous low-temperature properties of disordered materials were discovered and have been investigated experimentally primarily in classical glasses obtained by quenching from the melt. In this method of preparation the material inherits the basic elements of the disorder of the atomic structure of the liquid, manifested in universal low-temperature anomalies.

Besides the method of quenching from the liquid phase, a large number of methods of so-called solid-phase amorphization have recently been proposed. A common feature of all these methods is that the disordered state of the material is obtained at low tem-

peratures (room temperature and below) and, more importantly, from an initial crystalline state, bypassing the liquid phase. One method of solid-phase amorphization is pressure treatment. Bulk amorphous states of a number of semiconductors and insulators that cannot be quenched from the liquid phase have been obtained by this method.

However, despite the quite large number of works on solid-phase amorphization under high pressure, the study of the physical properties of the amorphous states obtained has concentrated mainly on the investigation of their transport characteristics.[5,6] There are no published data on the low-temperature thermophysical properties of such amorphous phases, making it impossible to compare with the similar properties of canonical glasses. An obvious question arises in this connection: To what degree are the physical properties of samples obtained by solid-phase amorphization under pressure identical to those of classical glasses obtained by quenching from the liquid phase?

To clarify this question we measured the low-temperature specific heat of crystalline and amorphous (obtained under pressure) $Eu_2(MoO_4)_3$.

Europium molybdate was chosen as the object of investigation on the basis of the following considerations. In Refs. 7–9 it was shown that many molybdates of rare-earth metals, $Gd_2(MoO_4)_3$, $Tb_2(MoO_4)_3$, $Sm_2(MoO_4)_3$, and $TbGd(MoO_4)_3$, become amorphous under pressure. However, in all these compounds the rare-earth cation possesses a substantial magnetic moment. For this reason, a considerable magnetic contribution to the specific heat can be expected at low temperatures, which complicates the analysis of the experimental data. The trivalent Eu ion has zero magnetic moment, and the compound $Eu_2(MoO_4)_3$ is isostructural for crystals of this series. It was natural to expect that europium molybdate would become amorphous for the same temperature–pressure parameters as other members of this family.

Solid-phase amorphization of $Eu_2(MoO_4)_3$ was performed by the pressure method described in Ref. 9. A polycrystalline sample of $Eu_2(MoO_4)_3$ was subjected to hydrostatic pressure to 7 GPa at room temperature. After holding the sample for 2 h under these conditions and then removing the pressure, a x-ray investigation of the sample was performed. The diffraction patterns obtained were typical for the amorphous state. The specific-heat measurements were performed in a relaxation-type calorimeter in the temperature interval 4.5–30 K. A description of our calorimetric method of measurement is given in Ref. 10.

Figure 1 displays the temperature dependences C_{total}/T^3. The experimentally measured specific heat C_{total} of crystalline and amorphous samples of $Eu_2(MoO_4)_3$ is shown in the inset in Fig. 1. The measured specific heat of the crystal (the curve ''cr'') at temperatures $T \leqslant 7.5$ K is described by a Debye-type cubic function $C_{\text{total}} = C_0 \cdot T^3$, where $C_0 \approx 1.06 \times 10^{-6}$ J/g·K^4, and therefore the Debye temperature is $\Theta_D \approx 126$ K.

The temperature dependence of C_{total}/T^3 for the amorphous material (the curve ''am'') differs considerably from the temperature dependence for the crystalline sample. A peak is present at temperature $T \approx 10$ K. The presence of such a peak is typical for various dielectric glasses.

As indicated above, all dielectric glasses exhibit universal anomalies at low temperatures. Two temperature intervals of the anomalies are ordinarily distinguished: $T \leqslant 1$ K and $1-3 < T < 30-50$ K. A general approach for describing the properties of glasses was given in Refs. 4 and 11–13, where double- and single-well potentials arising

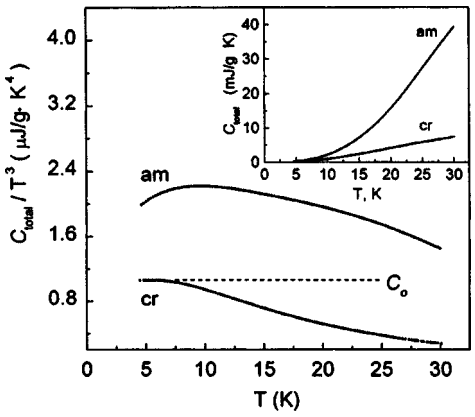

FIG. 1. C_{total}/T^3 versus temperature for crystalline (cr) and amorphous (am) samples of $Eu_2(MoO_4)_3$. The dashed line shows the value of the constant C_0 in the Debye law for a crystalline sample. Inset: Experimental curves $C_{\text{total}}(T)$.

as a result of a ''defect'' (local softening) of the elastic moduli was examined. The soft atomic potentials model proposed in these works made it possible to describe many properties of glasses over a wide temperature range.

In the present work the specific-heat measurements were performed in the temperature interval corresponding to the higher-temperature range of anomalies in glasses. For this temperature interval the soft atomic potentials model indicates the existence of other excitations besides phonons, viz., quasilocal harmonic oscillators. At temperatures of the order of several degrees Kelvin the density of states of these excitations is proportional to the fourth power of the energy, and the additional specific heat associated with them $C_{\text{ex}} \propto T^5$. The density of states of harmonic oscillators, which increases rapidly with energy, leads to the fact that at some energy E_d the harmonic oscillators become delocalized, their density of states becomes a linear function of the energy, and the specific heat $C_{\text{ex}} \propto T^2$. Therefore a peak appears in the function $C_{\text{ex}}/T^3 = (C_{\text{total}} - C_D)/T^3$ (where C_D is the phonon part of the specific heat) at $T_{\max} \approx E_d/5$.

Ordinarily, the experimental data on the elastic properties of the amorphous state are used to analyze the excess specific heat C_{ex} (Refs. 12 and 14). These data are used to calculate the value of C_0, and the difference $C_{\text{ex}} = C_{\text{total}} - C_0 \cdot T^3$ is taken as the value of the excess specific heat. The Debye temperature for $Eu_2(MoO_4)_3$ is low ($\Theta_D \approx 130$ K), and in this case such a calculation of C_{ex} becomes incorrect at temperatures $T > \Theta_D/10 \approx 13$ K. Moreover, at the present time there are no experimental data that would make it possible to calculate the Debye-law constant C_0. For this reason the experimental data were analyzed as follows. In the temperature range 4.5–7.5 K the specific heat of the crystal is proportional to the cubed temperature. Disordering results in softening of the elastic moduli and hence a decrease of the Debye temperature, so that the phonon part of the specific heat of the amorphous phase should also vary as T^3 at temperatures not exceeding 7.5 K. Besides phonons, at these temperatures harmonic excitations are also present in the amorphous phase. Their contribution to the specific heat is $\propto T^5$. Therefore the specific heat C_{total}/T^3 of the amorphous phase in the temperature interval 4.5–7.5 K can be described by the expression

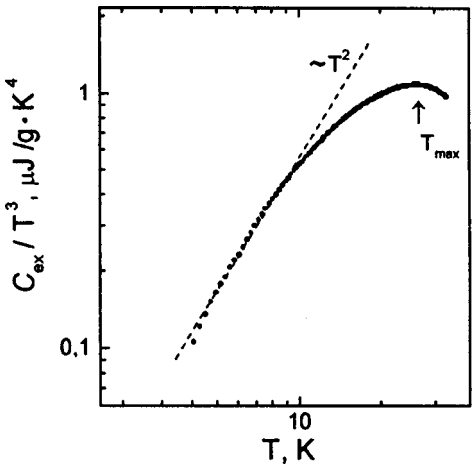

FIG. 2. Log–log plot of the temperature dependence of the excess specific heat C_{ex}/T^3 of the amorphous state. The dashed line shows the extrapolation $C_{ex} \propto T^5$.

$$C_{total} = C_0 \cdot T^3 + C_5 \cdot T^5. \quad (1)$$

Analysis of the experimental data using expression (1) gave the following values for the constants: $C_0 \approx 1.94 \times 10^{-6}$ J/g·K^4 and $C_5 \approx 4.71 \times 10^{-9}$ J/g·K^6. Therefore the value of C_0 for amorphous europium molybdate is higher than the analogous value for its crystalline modification. It should be noted that the contribution of harmonic excitations to the specific heat is quite considerable, and at $T = 7.5$ K it constitutes $\sim 14\%$ of the phonon contribution. The ratio of the average sound velocities in crystalline and amorphous europium molybdate can be estimated as $V_s^{cr}/V_s^{am} \approx 1.27$ from the analytical expression for C_0 and the experimental data[5] on the relative change in density $\Delta\rho/\rho \approx 0.14$ on amorphization of $Gd_2(MoO_4)_3$. This is a typical value for this ratio in canonical glasses.

We assumed that at temperatures above 7.5 K the phonon part of the specific heat in the amorphous phase exhibits the same functional dependence as in the crystal but multiplied by the ratio C_0^{am}/C_0^{cr}. Accordingly, the excess specific heat of the amorphous state for the entire interval of the measurements was determined as $C_{ex} = C_{total}^{am} - C_{total}^{cr}(C_0^{am}/C_0^{cr})$. A log–log plot of the temperature dependence of the quantity C_{ex}/T^3 is shown in Fig. 2. For C_{ex} extracted in this manner the peak is shifted to higher temperatures ($T_{max} \approx 24$ K) compared with its position in the dependence C_{total}^{am}/T^3 (Fig. 1, curve ''am''). As one can see from Fig. 2, the interval where $C_{ex} \propto T^5$ lies at temperatures $T \leqslant 9.5$ K, after which, up to the peak, the specific heat varies much more slowly with temperature. To the right of the peak the exponent in the temperature dependence of the specific heat becomes less than 3, in agreement with the soft atomic potentials model.

In summary, the characteristic features of the low-temperature specific heat of amorphous $Eu_2(MoO_4)_3$ are described well in the soft atomic potentials model developed for canonical glasses, and in this respect the product of solid-phase amorphization is similar to dielectric glasses obtained by quenching from the liquid.

We thank B. K. Ponomarev for a discussion of the results obtained in this work and for valuable remarks. Financial support was provided by Russian Fund for Fundamental Research through Grants Nos. 96-02-18545 and 96-15-96806.

[a)]e-mail: sinitsyn@issp.ac.ru

[1] R. C. Zeller and R. O. Pohl, Phys. Rev. B **46**, 2029 (1971).
[2] S. Hunklinger and A. K. Raychaudhuri, in *Progress in Low Temperature Physics*, edited by D. F. Brewer, Elsevier, Amsterdam, 1976, Vol. 9, p. 265.
[3] W. A. Phillips, Rep. Prog. Phys. **50**, 1657 (1987).
[4] Yu. M. Galperin, V. G. Karpov, and V. I. Kozub, Adv. Phys. **38**, 669 (1989).
[5] V. F. Gantmakher, V. N. Zverev, V. M. Teplinskiĭ, and O. I. Barkalov, Zh. Éksp. Teor. Fiz. **103**, 1460 (1993) [JETP **66**, 714 (1993)].
[6] V. F. Gantmakher, V. N. Zverev, V. M. Teplinskiĭ *et al.*, Zh. Éksp. Teor. Fiz. **104**, 3217 (1993) [JETP **77**, 513 (1993)].
[7] L. H. Brixner, Mater. Res. Bull. **7**, 879 (1972).
[8] A. Jayaraman, S. K. Sharma, Z. Wang *et al.*, J. Phys. Chem. Solids **54**, 827 (1993).
[9] E. G. Ponyatovskiĭ, V. V. Sinitsyn, R. A. Dilanyan, and B. S. Red'kin, JETP Lett. **61**, 222 (1995).
[10] A. V. Palnichenko, A. F. Gurov, V. N. Kopylov *et al.*, Phys. Rev. B **56**, 1 (1997).
[11] V. G. Karpov, M. I. Klinger, and F. N. Ignat'ev, Zh. Éksp. Teor. Fiz. **84**, 760 (1983) [Sov. Phys. JETP **57**, 439 (1983)].
[12] U. Buchenau, Yu. M. Galperin, V. L. Gurevich, and H. R. Schober, Phys. Rev. B **43**, 5039 (1991).
[13] D. A. Parshin, Fiz. Tverd. Tela (St. Petersburg) **36**, 1809 (1994) [Phys. Solid State **36**, 991 (1994)].
[14] G. Garini, G. D'Angelo, G. Tripodo *et al.*, Phys. Rev. B **52**, 9342 (1995).

Translated by M. E. Alferieff

Self-excitation of 2D plasmons in resonant tunneling diodes

M. N. Feĭginov[a)] and V. A. Volkov[b)]
Institute of Radio Engineering and Electronics, Russian Academy of Sciences, 103907 Moscow, Russia

(Submitted 11 September 1998)
Pis'ma Zh. Éksp. Teor. Fiz. **68**, No. 8, 628–633 (25 October 1998)

Resonant tunneling is accompanied by the accumulation of 2D electrons in the quantum well between the barriers of resonant tunneling diodes. In high-quality structures this gives a *Z*-shaped current–voltage characteristic, and it is shown that self-excitation of 2D plasmons occurs in this quantum well for any external circuit at completely realistic parameters of the structures. © *1998 American Institute of Physics.* [S0021-3640(98)00720-8]

PACS numbers: 85.30.Mn, 73.20.Dx, 73.20.Mf

Resonant tunneling diodes (RTDs) based on double-barrier semiconductor heterostructures ordinarily possess a *N*-shaped current–voltage (I–V) characteristic.[1] However, it was discovered ten years ago that the accumulation of 2D electrons in the quantum well of a RTD can change the I–V characteristic from *N*-type to *Z*-type.[2–6] In standard measurements (for example, in a fixed-voltage regime) this should be observed as current bistability. Recently an experimental method was proposed[7,8] by which negative load resistances are realized, making it possible to measure *Z*-type I–V characteristics. The interpretation of the results obtained in Refs. 7 and 8 depends on the solution of the problem of the stability of uniform (along the quantum well — QW) current and charge distributions in the RTD against nonuniform disturbances on the *Z*-shaped part of the I–V characteristic. The present letter is devoted to this problem. The problem is formulated in terms of 2D plasmons — low-frequency charge oscillations in the QW. In our view this language is best suited for the problem under study.

We note that the problem of the nonuniform nonlinear distribution of the tunneling current in a RTD was studied in Ref. 9. The results showed a complicated dependence on the parameters of the system. Unfortunately, the situation considered in Ref. 9 (very thin barriers and no external circuit) is inapplicable for describing the experiment of Refs. 7 and 8.

In the present letter the properties of 2D plasmons in the QW in a RTD are studied analytically. The screening of these plasmons by a high-conductivity emitter and collector is taken into account (it is well known[10] that in an ideal 2D gas the screening by a metal plane results in a linear plasmon spectrum $\omega(q)$). The problem of the linear stability of such plasmons is solved. The results are valid for arbitrary tunneling barriers

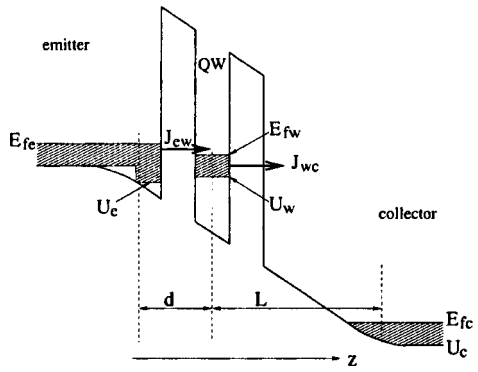

FIG. 1. Energy diagram of a RTD in the resonant tunneling regime. The 2D electron gas in the QW is formed by the balance of the resonant emitter–well current (J_{ew}), the nonresonant well–collector current (J_{wc}), and the spreading of 2D electrons along the well; see Eq. (2).

in the presence of an arbitrary external circuit. The parameters determining the instability are extracted from a comparison with experiment.

BASIC EQUATIONS

We shall consider a RTD (Fig. 1) in the sequential-tunneling model.[11] We assume that in the QW the electron lifetimes τ_e and τ_c due to tunneling into the emitter and collector, respectively, are long compared with the momentum relaxation time τ. This is virtually always the case (see estimates below). The system of equations describing the temporal and spatial (x,y) distribution of the currents in the QW consist of the constitutive relation (1), the continuity equation (2), and the Poisson equation in the local-capacitance approximation (3):

$$\frac{\partial \mathbf{J}}{\partial t}+\nu\mathbf{J}=\frac{\sigma\nu}{e}\nabla E_{fw}, \tag{1}$$

$$-e\frac{\partial}{\partial t}N_{2D}+\nabla\cdot\mathbf{J}=J_{ew}-J_{wc}, \tag{2}$$

$$V-V_0=\frac{e^2}{C}N_{2D}-(E^0_{fe}-E^0_{fc})\frac{d}{L+d}, \tag{3}$$

$$J_{ew}=-[E_{fe}-E_{fw}-(E_{fe}-U_w)\,\theta(U_w-E_{fe})]\rho_{2D}\frac{e}{\tau_e}\tilde{\theta}(V), \tag{4}$$

$$J_{wc}=-N_{2D}\frac{e}{\tau_c}, \tag{5}$$

where $\mathbf{J}(x,y)$ is the 2D current density in the QW; J_{ew} and J_{wc} are the z components of the emitter–well and well–collector current densities, respectively; $N_{2D}=[E_{fw}-U_w]\rho_{2D}$ is the local 2D-electron density in the QW; ρ_{2D} is the 2D density of states in the QW; E_{fi} and U_i are the local Fermi level and the band-bottom energy in the emitter near the barrier $(i=e)$, in the well $(i=w)$, and in the collector $(i=c)$; and, $V=U_w$

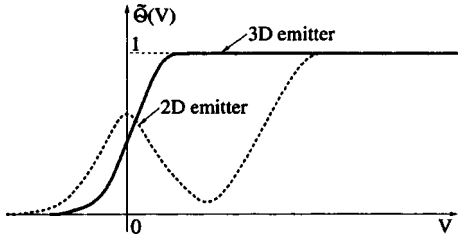

FIG. 2. Form factor of the broadening of the emitter–well resonant tunneling transitions as a function of V. Solid line — for transitions from a 3D emitter, dotted line — additional contribution of transitions from a 2D emitter (i.e., from the enrichment layer in Fig. 1).

$-U_e$. For simplicity it is assumed that at zero external bias the bottom of the 2D subband in the QW lies above the Fermi level in the emitter, in which case $V=V_0$; τ_e and τ_c are assumed to be independent of V, an assumption which is justified when a bending of the conduction-band bottom comparable in depth to E_{fw} is present near the emitter–barrier boundary. The effective emitter–well distance d is greater than the thickness of the emitter barrier by the Thomas–Fermi screening length and the half-width of the QW; L is the analogous well–collector distance, including additionally the length of the depletion region; $C=\epsilon(L+d)/4\pi Ld$ is the capacitance per unit area of the QW, $\nu=1/\tau$, $\sigma=N_{2D}e^2/m^*\nu$ is the static 2D conductivity of the QW. The form factor $\tilde{\theta}(V)$ describes the broadening of the resonance levels due to emitter–well transitions (Fig. 2). We note that, neglecting the level broadening, for transitions from a 3D emitter $\tilde{\theta}(V)$ is a step function $\theta(V)$. The local-capacitance approximation is valid when the scale of the nonuniformities in the plane of the QW is large compared with d and L. We shall represent the solution of the system (1)–(5) in the form of a uniform static solution (superscript 0) plus small fluctuations: $V=V^0+\delta V(x,y)$, $N_{2D}=N_{2D}^0+\delta N_{2D}(x,y)$, $E_{fi}=E_{fi}^0+\delta E_{fi}(x,y)$, and so on.

UNIFORM NONLINEAR STATIC SOLUTION

Neglecting all derivatives in Eqs. (1)–(5) we obtain

$$V^0-V_0-\frac{e^2N_{2D}^0}{C}=-(E_{fe}^0-E_{fc}^0)\frac{d}{L+d}, \tag{6}$$

$$N_{2D}^0=\rho_{2D}\frac{[E_{fe}^0-U_e^0-V^0]\tilde{\theta}(V^0)/\tau_e}{1/\tau_c+\tilde{\theta}(V^0)/\tau_e}\,\theta(E_{fe}^0-U_e-V^0), \tag{7}$$

$$J_{wc}^0=J_{ew}^0=-\frac{eN_{2D}^0}{\tau_c}. \tag{8}$$

The third term on the left-hand side of Eq. (6) describes the Coulomb interaction of the electrons in the well with the emitter and collector. As a result of this term, the solution (6) and (7) for the function $V^0(E_{fe}^0-E_{fc}^0)$ is multivalued on the Z-shaped part of the I–V characteristic, i.e., the V^0 derivative of the left-hand side of Eq. (6) is negative (if Coulomb effects were neglected, this derivative would be positive) on the central leg of the I–V characteristic:

$$1+\frac{e^2\rho_{2D}}{C\tau_e}\frac{1}{1/\tau_c+\tilde{\theta}(V^0)/\tau_e}\left[\tilde{\theta}(V^0)-\frac{[E_{fe}^0-U_e^0-V^0]\tilde{\theta}'(V^0)}{1+\tilde{\theta}(V^0)\tau_c/\tau_e}\right]<0. \tag{9}$$

2D-PLASMON SPECTRUM

Linearizing the system of equations (1)–(5) around the uniform stationary solution (6)–(8) yields an equation describing screened 2D plasmons in the RTD:

$$\left[\left(\nu+\frac{\partial}{\partial t}\right)\left(\nu_T+\frac{\partial}{\partial t}\right)-\frac{\sigma^0\nu}{C}\left(1+\frac{C}{e^2\rho_{2D}}\right)\nabla^2\right]\delta N_{2D}(x,y)=0, \tag{10}$$

where

$$\nu_T=\frac{1}{\tau_c}+\frac{\tilde{\theta}(V^0)}{\tau_e}+\frac{e^2\rho_{2D}}{C}\left[\frac{\tilde{\theta}(V^0)}{\tau_e}-\frac{[E_{fe}^0-U_e^0-V^0]}{1+\tilde{\theta}(V^0)\tau_c/\tau_e}\frac{\tilde{\theta}'(V^0)}{\tau_e}\right] \tag{11}$$

is, physically, the tunneling-relaxation rate of the charge in the QW. The first and second terms in Eq. (11) describe relaxation due to electron tunneling into the collector and emitter, respectively. As E_{fw} varies, the energy of the bottom of the 2D subband in the QW also shifts as a result of the Coulomb interaction of the electrons in the well with the emitter and collector. In the presence of such a shift the current J_{ew} acquires an additional contribution due to the change in the number of free states in the QW which are accessible for tunneling (this mechanism is described by the third term). This current varies as a result of the form factor $\tilde{\theta}(V)$, and effect which is described by the fourth term in Eq. (11). The factor in front of the brackets in Eq. (11) equals $\delta U_w/\delta E_{fw}$. The factor in front of $\tilde{\theta}'(V^0)/\tau_e$ is the difference of the Fermi levels of the emitter and the well, and $\tilde{\theta}'$ is the derivative of the form factor.

Equation (10) implies the dispersion relation

$$(\omega+\imath\nu)(\omega+\imath\nu_T)=\frac{\sigma^0\nu}{C}\left(1+\frac{C}{e^2\rho_{2D}}\right)q^2 \tag{12}$$

for the 2D-plasmon spectrum . The solution of Eq. (12) increases in time (unstably) in the region of 2D wave numbers q in which $\mathrm{Im}\,\omega(q)>0$. One can see from Fig. 3 that 2D plasmons are unstable only if $\nu_T<0$. A comparison of Eqs. (11) and (9) shows that one always has $\nu_T<0$ on the central leg of the *Z*-shaped I–V characteristic. For $-\nu_T>\nu$ the 2D plasmons are unstable for any q. Traveling solutions for which $\mathrm{Re}\,\omega\neq 0$ are also unstable. For $-\nu<\nu_T<0$ the plasmons are unstable only if $q<q_0$, where

$$q_0=\sqrt{-\frac{\nu_T C}{\sigma^0}\left(1+\frac{C}{e^2\rho_{2D}}\right)^{-1}}. \tag{13}$$

Let us now examine how the stability of 2D plasmons is affected by the finite dimensions of the RTD in the (x,y) plane. We shall find the solution of Eq. (10) with the boundary condition that the normal component (i.e., normal to the lateral surface) of the current in the 2D layer of the structure vanishes (in nonuniform structures other boundary conditions are also possible; see Ref. 9). For a structure in the form of a strip ($|x|\leqslant W$) of width $2W$ we obtain the condition of quantization of the wave number

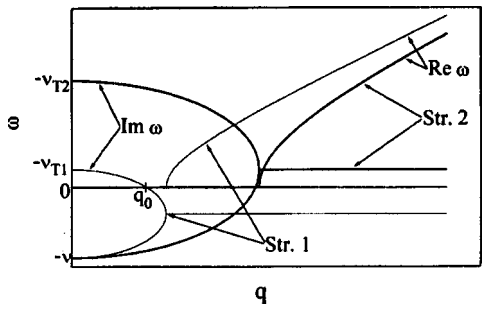

FIG. 3. Complex frequency of screened 2D plasmons in a RTD versus the wave number q in the QW plane. In the DBHS1 structure $-\nu<\nu_T<0$, while in the DBHS2 structure $-\nu_T>\nu$. Plasmons are unstable in the region Im $\omega>0$.

$$q_x=\frac{\pi}{2W}N, \tag{14}$$

i.e., an integer number ($N=1,2,3,\ldots$) of plasmon half wavelengths should fit within the width of the structure (only solutions which are uniform in the y direction are considered). The uniform solution (with $N=0$) must be studied separately; its stability is determined by the external circuit (an external circuit with a negative load resistance enables making this solution stable on the Z-shaped part of the I–V characteristic[7]). Therefore for $-\nu<\nu_T<0$ the instability of 2D plasmons can be suppressed by decreasing W: for

$$q_0<\frac{\pi}{2W} \tag{15}$$

2D plasmons with $N\neq 0$ will be stable. However, for $-\nu_T>\nu$ the 2D plasmons are unstable for any q, and traveling modes for which Re $\omega\neq 0$ are excited.

ESTIMATES

We shall present estimates of the characteristic parameters ν_T and q_0 for the RTDs in Ref. 12 (a) and Refs. 7 and 8 (b).

a) The thin-barrier RTD from Ref. 12 for high-frequency applications has thin AlAs (1.5 nm) barriers, a GaAs well (4.5 nm), and $d\approx 10$ nm. On the descending part of the I–V characteristic $L\approx 70$ nm and $V^0\approx 0$. A self-consistent calculation of the energy diagram[12] gives $E^0_{fe}-U^0_e\approx 100$ meV. With the use of Eqs. (7) and (8), the value $1/\tau_e \approx 1/\tau_c\approx 1.6\times 10^{11}\ \mathrm{s}^{-1}$ can be extracted from the maximum current density 4×10^4 A/cm^2 measured at room temperature. To estimate ν_T we shall assume that the broadening of the tunneling transitions $\tilde{\theta}(V^0)/\tilde{\theta}'(V^0)\approx 7$ meV, with $\tilde{\theta}(V^0)\approx 0.3$. Then $\nu_T\approx -60/\tau_c\approx -10^{13}\ \mathrm{s}^{-1}$. An estimate of ν follows from the values of the 2D mobility in a QW: In high-quality structures at room temperature $\mu\approx 3\times 10^3$ cm^2/V·s, which corresponds to $\nu\approx 10^{13}\ \mathrm{s}^{-1}$. Then $\nu_T\approx -\nu$. For high values of the mobility or smaller broadening of the resonant tunneling transitions, 2D plasmons will self-excite in RTDs of any dimensions.

b) In Refs. 7 and 8 a *Z*-shaped I–V characteristic in a structure with thick $Ga_{0.6}Al_{0.4}As$ barriers (8.3 nm and 11.1 nm) was measured at low temperatures. Its parameters are presented in Ref. 13: $\tau_c = 6\times10^{-7}$ s, $\tau_e \ll \tau_c$, $N^0_{2D,\max} = 2\times10^{11}$ cm^{-2}, $d \approx 10$ nm, $L \gg d$. For estimation we take $\tilde{\theta}(V^0) \approx 0.3$ and assume a level broadening $\tilde{\theta}(V^0)/\tilde{\theta}'(V^0) \approx 1$ meV. Then $\nu_T \approx -200/\tau_c \approx -10^8$ s^{-1}. Since for reasonable values of the 2D mobility the condition $|\nu_T| \ll \nu$ is satisfied, only modes with $q < q_0$, where $q_0 \approx 7\times10^{-2}\mu$m^{-1} with $\mu = 3\times10^3$ cm^2/V·s, are unstable. It follows from Eq. (15) that 2D plasmons are unstable for RTDs in the form of a strip of width $2W > 50\mu$m. This is also true for the large-diameter (200 μm) RTDs used in Refs. 7 and 8.

CONCLUSIONS

We have found the spectrum of screened 2D plasmons in the quantum well of a RTD in the resonance-tunneling regime and have investigated the properties of the plasmons. In high-quality structures the ''bare'' static I–V characteristic has a *Z*-shaped part, whose central leg is always unstable against the excitation of 2D plasmons with arbitrary or quite small wave numbers. One of three cases is realized in RTDs with a strip mesa of width $2W$:

1. Low-quality structures (large broadening of resonance transitions). In these structures $\nu_T > 0$, the I–V characteristic is *N*-shaped, and 2D plasmons are stable in the present model. Nonetheless, fluctuations of the QW thickness can in principle lead to 2D plasma instability even if the average I–V characteristic is *N*-shaped.

2. High-quality structures (small broadening of resonance transitions) with thick tunneling barriers. For these structures $\nu_T < 0$ and the I–V characteristic has a *Z*-shaped part. On account of the low barrier transmittance $-\nu_T < \nu$. As a result, 2D-plasma instability develops only large RTDs ($2W > \pi/q_0$). For small $2W$ this instability is suppressed by electron scattering.

3. High-quality structures ($\nu_T < 0$) with thin barriers. In this case $-\nu_T > \nu$, and the central leg of the I–V characteristic is unstable for RTDs of any size.

Self-excitation of 2D plasmons should be reflected in the measured I–V characteristics. Preliminary results[14] indicate that the experimental data of Refs. 7 and 8 can be explained on the basis of this mechanism.

This work was supported in part by the Russian Fund for Fundamental Research (Project No. 96-02-18811), the program ''Physics of Solid-State Nanostructures'' of the Ministry of Science (Project No. 1-094/4), INTAS-RFBR (Nos. 95-0849 and 97-1475), and CRDF (RC1-202).

[a)]e-mail: misha@mail.cplire.ru
[b)]e-mail: VoVA@mail.cplire.ru

[1] H. Mizuta and T. Tanoue, *The Physics and Applications of Resonant Tunneling Diodes*, Cambridge University Press, 1995.
[2] F. W. Sheard and G. A. Toombs, Appl. Phys. Lett. **52**, 1228 (1988).
[3] V. J. Goldman, D. C. Tsui, and J. E. Cunningham, Phys. Rev. Lett. **58**, 1256 (1987).
[4] A. Zaslavsky, V. J. Goldman, D. C. Tsui, and J. E. Cunningham, Appl. Phys. Lett. **53**, 1408 (1988).
[5] R. K. Mains, J. P. Sun, and G. I. Haddad, Appl. Phys. Lett. **55**, 371 (1988).
[6] H. L. Berkowitz and R. A. Lux, J. Vac. Sci. Technol. B **5**, 967 (1987).

[7] A. D. Martin, M. L. Lerch, P. E. Simmonds, and L. Eaves, Appl. Phys. Lett. **64**, 1248 (1994).
[8] C. Zhang, M. L. F. Lerch, A. D. Martin *et al.*, Phys. Rev. Lett. **72**, 3397 (1994).
[9] B. A. Glavin, V. A. Kochelap, and V. V. Mitin, Phys. Rev. B **56**, 13346 (1997).
[10] A. V. Chaplik, Zh. Éksp. Teor. Fiz. **62**, 746 (1972) [Sov. Phys. JETP **35**, 395 (1972)].
[11] S. Luryi, Appl. Phys. Lett. **47**, 490 (1985).
[12] E. R. Brown, T. C. L. G. Sollner, W. D. Goodhue, and C. D. Parker, Appl. Phys. Lett. **50**, 83 (1987).
[13] M. L. Leadbeater, E. S. Alves, F. W. Sheard *et al.*, J. Phys.: Condens. Matter **1**, 10605 (1989).
[14] M. N. Feiginov and V. A. Volkov, in *Abstracts of the 24th International Conference on the Physics of Semiconductors*, Jerusalem, Israel, Tu-P101 (1998).

Translated by M. E. Alferieff

Magnetoexcitons in type-II quantum dots

A. B. Kalameĭtsev[a)] and V. M. Kovalev
Institute of Semiconductor Physics, Russian Academy of Sciences, 630090 Novosibirsk, Russia

A. O. Govorov
Institute of Semiconductor Physics, Russian Academy of Sciences, 630090 Novosibirsk, Russia; Center for Nanoscience and Sektion Physik, Ludwig-Maximilians-Universität, D-80539 München, Germany

(Submitted 21 September 1998)
Pis'ma Zh. Éksp. Teor. Fiz. **68**, No. 8, 634–637 (25 October 1998)

The ground state of a spatially indirect exciton in type-II quantum dots with a short-range potential acquires nonzero angular momentum in the presence of a magnetic field oriented perpendicular to the plane of the system. The critical magnetic field of the transition to a ground state with nonzero angular momentum depends on the radius of the quantum dot. Such a transition can be observed as quenching of luminescence by a magnetic field in quantum dots of the GaSb/GaAs system, for example. © *1998 American Institute of Physics.*
[S0021-3640(98)00820-2]

PACS numbers: 71.35.Ji, 73.20.Dx

Type-II quantum dots are formed in the GaSb/GaAs system.[1] In such quantum dots a three-dimensional quantum well exists only for holes, while a potential barrier exists for electrons. Spatially indirect excitons localized near quantum dots exist in this system.[1] The indirect excitons were observed in the luminescence spectra.[1]

The ground state of an exciton in two-dimensional quantum wells[2] and in type-I quantum dots with cylindrical symmetry[3] possesses zero angular momentum for any value of the magnetic field. Exciton localization in microstructures with a complicated geometry can lead to interesting effects.[4,5] For example, the energy of an exciton in a quantum ring oscillates as the magnetic field increases.[5]

In the present letter we investigate excitons localized near a type-II quantum dot. We show that the angular momentum of such an exciton in the ground state varies as a function of the magnetic field. This effect can be observed as quenching of luminescence. We note that in most cases a magnetic field increases the probability of an interband transition (see, for example, Refs. 2 and 3), and it intensifies the luminescence on account of compression of the wave function. The change in the ground state can be demonstrated in the model shown in Fig. 1. The system consists of a two-dimensional AlGaAs/GaAs/AlGaAs quantum well containing a built-in quantum dot in the form of a GaSb cylinder of radius r_0 and height L. The band diagram is shown in Fig. 1b. Similar systems have been investigated experimentally in Ref. 1.

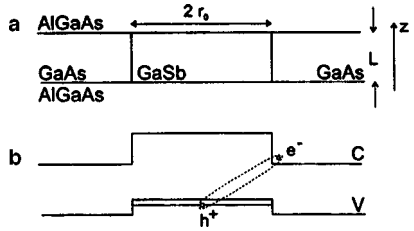

FIG. 1. Structure and band diagram for a GaSb–GaAs type quantum dot.

The motion of particles in such a system is assumed to be two-dimensional. The penetration of particles into the AlGaAs barriers will be neglected. The electron (hole) wave functions can be written in the form

$$\Psi_{e(h)}(\rho,\phi,z)=e^{il_{e(h)}\phi}R_{e(h)}(\rho)\psi(z), \tag{1}$$

where $(\rho,\phi)=\mathbf{r}$ are the coordinates in the plane of the system, $l_{e(h)}$ are the angular momenta, $R_{e(h)}(\rho)$ are the radial wave functions, and $\psi(z)$ is the size-quantization wave function in a square quantum well. An electron is localized near the quantum dot on account of attraction to the hole and moves in the potential shown in the inset in Fig. 2.

The probability of deexcitation of an exciton is determined by the integral

$$I=\int \Psi_e(\mathbf{R})\Psi_h(\mathbf{R})\,d\mathbf{R}=\int e^{i(l_e+l_h)\phi}\,d\phi\left[\int R_e(\rho)R_h(\rho)\rho\,d\rho\right]\int \psi^2(z)\,dz, \tag{2}$$

where $\mathbf{R}=(\mathbf{r},z)$.

The overlap integral $I_\rho=\int R_e(\rho)R_h(\rho)\rho d\rho$ of the radial wave functions is comparatively small because of the high potential barriers between GaAs and GaSb and varies smoothly as the magnetic field $\mathbf{B}\parallel\mathbf{z}$ increases. The factor that can change abruptly as a

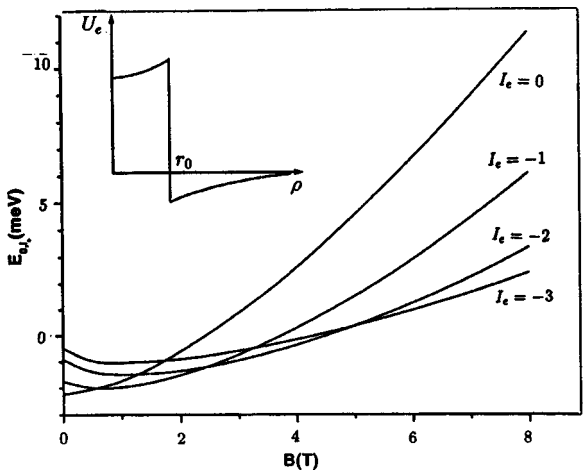

FIG. 2. Electron energy E_{0,l_e} versus the magnetic field for a quantum dot with $r_0=100$ Å and $L=70$ Å; $M_e=0.067m_0$. Inset: U_e versus ρ.

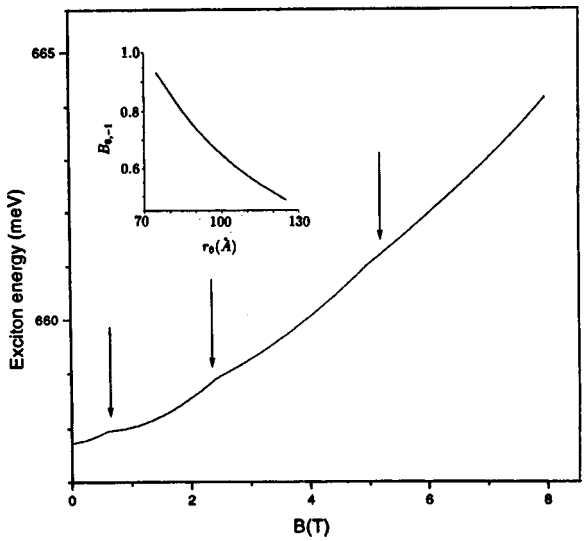

FIG. 3. Ground-state energy of an interband indirect exciton as a function of the magnetic field for a quantum dot with $r_0=100$ Å and $L=70$ Å; hole mass $M_h=0.3m_0$. The arrows show the change in angular momentum. Inset: Magnetic field $B_{0,-1}$ versus r_0.

function of B is the integral $I_\phi=\int e^{i(l_e+l_h)\phi}d\phi=2\pi\delta_{l_e+l_h}$, where $l_{e(h)}$ is the angular momentum of the ground state. If the total angular momentum of an exciton in the ground state is $l_e+l_h\neq 0$, then it does not contribute to luminescence. In the presence of rapid energy relaxation of excitons into the ground state at low temperature, the appearance of a situation with $l_e+l_h\neq 0$ signifies quenching of luminescence.

To demonstrate this effect we shall assume, to simplify the calculations, that particles do not penetrate through the GaSb–GaAs heterointerface, i.e., $R_{e(h)}(r_0)=0$. Since the penetration is small, this will not change the spectrum of the exciton much.[b)] Our estimates show that for dots of radius $r_0\sim 100$ Å the hole quantization can be assumed to be quite strong and the effect of the Coulomb interaction with an electron on the hole spectrum can be neglected. The wave function of the ground state of a hole with a flat bottom and impenetrable walls can be easily found, and for it $l_h=0$ for any B. The potential for an electron in the region $\rho>r_0$ is determined by the attraction to a hole:

$$U_e(\rho_e)=-\frac{e^2}{\epsilon}\int\frac{\psi^2(z_e)\psi^2(z_h)\,dz_e\,dz_h}{\sqrt{(\mathbf{r}_e-\mathbf{r}_h)^2+(\mathbf{z}_e-\mathbf{z}_h)^2}}R_h^2(\rho_h)\,d\mathbf{r}_h\,, \tag{3}$$

(see inset in Fig. 2). The quantization equation for $R_e(\rho)$ has the standard form

$$-\frac{\hbar^2}{2M_e}\left[R_e''+\frac{R_e'}{\rho}-\frac{l_e^2}{\rho^2}R_e\right]+\left(\frac{\hbar\omega_c}{2}l_e+\frac{M_e\omega_c^2}{8}\rho^2+U_e(\rho)\right)R_e=ER_e\,, \tag{4}$$

where ω_c is the electron cyclotron frequency and M_e is the electron effective mass. The spectrum has two quantum numbers n and l_e. In the ground state $n=0$ always. Figure 2 shows the numerical results for E_{0,l_e}. One can see that the angular momentum of the ground state varies with the magnetic field. The magnetic field $B_{0,-1}$ at which the

changeover $l_e=0\rightarrow l_e=-1$ of the ground-state angular momentum occurs depends on r_0 (see inset in Fig. 3). The ground-state energy of an exciton is displayed in Fig. 3 and has a kink on account of the change in the angular momentum. The energy of the exciton was calculated for a quantum dot with a sharp GaSb–GaAs heterointerface. In the experiments of Ref. 1 the energies of indirect excitons lie much higher (~ 1 eV) on account of diffusion of Sb into GaAs. The angular momentum of the ground state changes from l_e to l_e-1 when $r_0^2/l_c^2\sim l_e$, where l_c is the magnetic length. This follows from an analysis of the character of the wave function in a magnetic field. The changeover of the ground state is analogous to the appearance of a nondecaying current in the ground state in rings carrying electrons[6] and charged excitons.[7] The present letter is concerned with the case of a quasiparticle which is neutral as a whole but is polarized by the potential of the quantum dot. This polarization leads to the nondecaying current in the ground state. We note that the possibility of a situation where excitons would be optically inactive in the ground state was discussed in Ref. 8. In Ref. 8 excitons in crossed magnetic and electric fields were studied. It is easy to calculate the spectrum of an exciton for a finite barrier between GaAs and GaSb. In this case the character of the spectrum remains the same (see Fig. 2).

We thank A. V. Chaplik for helpful discussions. This work was supported by a grant from FOROPTO (Bavaria).

[a)]e-mail: kalam@isp.nsc.ru

[b)]Obviously, the penetration of the particles must be taken into account in the calculation of the intensity of an interband transition.

[1] F. Hatami, N. N. Ledentsov, M. Grundmann *et al.*, Appl. Phys. Lett. **67**, 656 (1995); F. Hatami, M. Grundmann, N. N. Ledentsov *et al.*, Phys. Rev. B **57**, 4635 (1998).
[2] I. V. Lerner and Yu. E. Lozovik, Zh. Éksp. Teor. Fiz. **78**, 1167 (1980) [Sov. Phys. JETP **51**, 588 (1980)].
[3] V. Halonen, T. Chakraborty, and P. Pietiläinen, Phys. Rev. B **45**, 5980 (1992).
[4] A. O. Govorov and A. V. Chaplik, Zh. Éksp. Teor. Fiz. **99**, 1853 (1991) [Sov. Phys. JETP **72**, 1037 (1991)].
[5] A. V. Chaplik, JETP Lett. **62**, 900 (1995).
[6] R. Landauer and M. Büttiker, Phys. Rev. Lett. **54**, 2049 (1985).
[7] A. O. Govorov and A. V. Chaplik, JETP Lett. **66**, 454 (1997).
[8] A. Imamoglu, Phys. Rev. B **54**, 14285 (1996).

Translated by M. E. Alferieff

Mesoscopic superconductivity in superspace

A. F. Andreev

P. L. Kapitsa Institute of Physics Problems, Russian Academy of Sciences, 117334 Moscow, Russia

(Submitted 24 September 1998)
Pis'ma Zh. Éksp. Teor. Fiz. **68**, No. 8, 638–642 (25 October 1998)

In the theory of mesoscopic superconductivity it is necessary to supplement the coordinates x,y,z with some additional physical characteristics (coordinates) of free space. An adequate description of mesoscopic superconductivity is obtained by introducing a nonrelativistic version of Grassmann spinor coordinates, which are studied in supersymmetric field theories and convert ordinary space into superspace. An experimental check of the proposed description of the superconducting and magnetic properties of metallic nanoparticles would provide a direct confirmation of the concept of superspace. © *1998 American Institute of Physics.* [S0021-3640(98)00920-7]

PACS numbers: 74.20.−z, 73.20.Dx, 74.25.Ha, 11.30.Pb

The unique nature of superconductivity in mesoscopic quantum dots (MQDs), i.e., in systems with a large number of electrons under conditions such that the temperature, the superconducting transition temperature, and other characteristic energy parameters are much smaller than the energy difference between the first excited and ground states of a system with a fixed number of particles, has been demonstrated in Refs. 1 and 2. Under these conditions the degrees of freedom associated with the motion of particles in space can be assumed to be completely frozen. Actually, the question concerns metallic nanoparticles of the type obtained by Ralph *et al.*[3] As noted previously,[1,2] the realizability of superconducting states in MQDs implies a change in the physical notions about the properties of space–time, since superconducting states, generally speaking, change physically under spatial rotations by 2π. If the standard coordinates x,y,z are exhaustive characteristics of space, then rotation by the angle 2π is simply an identity transformation under which nothing can change physically. The realizability of mesoscopic superconductivity therefore requires the introduction of additional physical characteristics (coordinates) of space. An alternative viewpoint, based on the introduction of superselection rules,[4] as shown in Refs. 1 and 2, is unsatisfactory. The additional coordinates must change under rotations by the angle 2π in order to make such rotations physically distinguishable from the identity transformation. Therefore they must correspond to a spinor representation of the rotation group.

We show below that a completely adequate description of mesoscopic superconductivity obtains if a nonrelativistic version of Grassmann (anticommuting) spinor coordinates, which are introduced in supersymmetric field theories and transform ordinary space into superspace, is introduced as additional coordinates. In MQDs conditions are

such that all degrees of freedom of the system, except those that correspond to motion along the additional coordinates, can be treated as frozen. An experimental check of the quantitative description formulated in this letter for the superconducting and magnetic properties of MQDs would therefore give a confirmation of the concept of superspace by means of an essentially direct experimental study of the dynamics of MQDs along the additional coordinates.

1. The specific nature of the thermodynamic behavior of MQDs lies in the fact[1,2] that a change in the average number $\langle N\rangle$ of electrons accompanying a change of their chemical potential occurs as a result of first-order phase transitions between phases characterized by different integral values of N. The states belonging to regions of coexistence of different phases and characterized by nonintegral $\langle N\rangle$ are superconducting. A general property of systems of Fermi particles is the parity effect (PE) — the difference of the quasicontinuous (for large N) functions $E_e(N)$ and $E_o(N)>E_e(N)$ giving the ground-state energy for even and odd N, respectively. Let us write the particle-number operator N in the form $N=N_e+n$, where N_e runs through all even numbers, while $0\leqslant n\leqslant 2$. There exist three phases for each N_e: I, II, and III with $n=0,1$, and 2, respectively. For a weak PE there are two critical values of the chemical potential $\mu_{c1}(N_e)$ and $\mu_{c2}(N_e)$ which correspond to the phase transitions I$\rightarrow$II and II$\rightarrow$III and coexistence of the phases (I, II) and (II, III). As the PE increases, the quantities μ_{c1} and μ_{c2} approach one another, so that for a certain definite magnitude of the PE there exists a triple point where all three phases exist simultaneously and $\mu_{c1}=\mu_{c2}$. For an even larger PE there is only one critical value $\mu_c(N_e)$ for the transition I$\rightarrow$III and coexistence of the phases (I, III). A situation where both cases (two transitions at μ_{c1} and μ_{c2} or one transition at μ_c for fixed N_e) occur in the same system for different values of N_e is possible (it has actually been realized experimentally[5]). In such a system there exists a triple point with N_e determined by the equation $\mu_{c1}(N_e)=\mu_{c2}(N_e)$.

2. The states of phase II with $n=1$, i.e., with an odd number of electrons in the absence of an external magnetic field (see Ref. 2), are magnetic. In the simplest case they correspond to a total spin 1/2 of the system, though in principle larger half-integer values 3/2, ... are also possible. The superconducting states, in which this ''one-fermion'' phase is present as one of the coexisting phases, change physically under spatial rotations by 2π. In accordance with what we have said above, to describe them it is necessary to introduce, together with coordinates x,y,z, additional Grassmann coordinates θ_α, $\overline{\theta^\alpha}\equiv\theta_\alpha^+$, where

$$\{\theta_\alpha,\theta_\beta\}=\{\overline{\theta^\alpha},\theta_\beta\}=\{\overline{\theta^\alpha},\overline{\theta^\beta}\}=0,$$

$\{\ldots,\ldots\}$ is an anticommutator, and $\alpha=1,2$ is a spinor index.

The dynamics of the system in the additional coordinates is described by quantum-mechanical operators $a_\alpha,\overline{a^\alpha}=a_\alpha^+$ satisfying the canonical relations

$$\{a_\alpha,a_\beta\}=\{\overline{a^\alpha},\overline{a^\beta}\}=0,\quad \{\overline{a^\alpha},a_\beta\}=\delta_\beta^\alpha. \tag{1}$$

Transformations of the $SU(2)$ group of spin rotations are generated by Hermitian spin operators $\mathbf{s}=(1/2)a_\alpha^+\boldsymbol{\sigma}_{\alpha\beta}a_\beta$, where $\boldsymbol{\sigma}_{\alpha\beta}$ are Pauli matrices. The gauge transforma-

tions $a_\alpha \to a_\alpha e^{i\phi}$, where ϕ is a constant, are generated by the Hermitian operator $n = \overline{a^\alpha} a_\alpha = a_\alpha^+ a_\alpha$, which is invariant under $SU(2)$ and must be identified as the operator $n \equiv N - N_e$ introduced above.

It is important to underscore that the universal description by means of the operators a_α is possible only when the ''purely Bose'' degrees of freedom of the system are completely frozen. For example, if the total spin of a one-fermion ($n=1$) state is 3/2, then since the spin 3/2 is a combination of spin 1/2 and the Bose spin 1, such a state is ''incompletely frozen'' with respect to the Bose degrees of freedom.

Despite the relation (1), the operators a_α and a_α^+ are not, generally speaking, annihilation and creation operators for any real particles. They represent universal characteristics of any system with an average number of fermions that is not an even integer under conditions such that the Bose degrees of freedom are completely frozen. In exactly the same manner, the conventional canonically conjugate coordinate and momentum operators describe the dynamics of a system with respect to a collective Bose variable under conditions such that all other degrees of freedom are frozen. The operators a_α and a_α^+ are therefore a generalization of the Pauli operators $\boldsymbol{\sigma}_{\alpha\beta}$ to the case where, together with x, y, and z, there exist additional coordinates θ_α.

3. The Hamiltonian of a nonrelativistic isolated system should be invariant under the spin rotations in $SU(2)$ and gauge transformations. The most general such Hamiltonian is

$$H_0 = \xi_1 - \frac{1}{2}(3\xi_1 + \xi_2)\hat{n} + \frac{1}{2}(\xi_1 + \xi_2)\hat{n}^2, \tag{2}$$

where ξ_1 and ξ_2 are constants. The origin of the energy coordinate is chosen so that $E_0 = 0$ for $n=1$, where the energy is represented by the quantity $E - \mu N$, which in equilibrium possesses a minimum for fixed μ.

In the occupation-number representation $|n_1, n_2\rangle$, where $n_1 = a_1^+ a_1$ and $n_2 = a_2^+ a_2$, there are four states $|0,0\rangle, |1,0\rangle, |0,1\rangle$, and $|1,1\rangle$ with the energies ξ_1, 0,0, and ξ_2, respectively.

In the general case the system possesses degrees of freedom which are not frozen at quite low temperatures, if $\xi_1 > 0$ and $\xi_2 > 0$, i.e., when the ground state corresponds to phase II with $n=1$. The most general Hamiltonian that depends on the operators a_α and a_α^+ and possesses transitions only between the degenerate states $|1,0\rangle$ and $|0,1\rangle$ in an isolated system has the form

$$H_B = -\mu_B \mathbf{B} \cdot a_\alpha^+ \boldsymbol{\sigma}_{\alpha\beta} a_\beta. \tag{3}$$

Here μ_B is the effective magnetic moment, which for a system of nonrelativistic electrons equals the Bohr magneton, and **B** is the magnetic field acting on the system. This field might be an external field or an effective internal field in the system MQD + contacts (see Ref. 2), which give rise to a magnetism of phase II in the absence of an external field. Therefore in the general case considered one can speak only of purely spin degrees of freedom.

4. Near a triple point of phase coexistence one has $\xi_1 \to 0$ and $\xi_2 \to 0$, and all four states are close in energy. The most general Hamiltonian has the form

$$H = H_0 + H_B + H_\Delta + H_\varphi + H_\psi, \tag{4}$$

where

$$H_\Delta = (1/2)\Delta^\alpha a_\alpha + \text{H.c.}, \quad H_\varphi = \varphi^\alpha n a_\alpha + \text{H.c.}, \quad H_\psi = \psi a_2 a_1 + \text{H.c.}$$

Here, once again, the quantities $\Delta^\alpha, \varphi^\alpha$, and ψ might be effective internal fields in the system MQD + contacts (see Refs. 1 and 2 and below), which give rise to superconductivity in a pair ''condensate'' (ψ) or with a single-electron ''condensate'' (Δ and φ). These quantities might also be proximity fields produced by superconductors of the appropriate type which possess higher values of the critical parameters and which are connected with the MQD under study by a tunneling contact. The field φ^α can be neglected, since it possesses the same symmetry as Δ^α but is due to low-probability multiple-particle tunneling processes. For the same reason, the field Δ^α, if it is nonzero, should be more important than ψ.

The Hamiltonian (4) is a generalization of the Pauli Hamiltonian (3) to a small neighborhood of the triple point, where the coordinates θ_α are almost completely free.

Since Δ^α transforms under spin rotations as a spinor of rank 1, it is always possible to obtain $\Delta^2 = 0$ by appropriately orienting the z axis. Then $\Delta^1 \equiv \Delta$ can be made to be positive by an appropriate rotation around the z axis. Setting $\varphi^\alpha = \psi = 0$ and switching to a matrix representation, in which the states $|n_1 n_2\rangle$ are written in the form of vertical columns

$$|0,0\rangle = (1000)^T, \quad |1,0\rangle = (0100)^T, \quad |0,1\rangle = (0010)^T, \quad |1,1\rangle = (0001)^T,$$

where T indicates transposition, we write the Hamiltonian in the matrix form

$$H = \begin{pmatrix} \xi_1 & \Delta/2 & 0 & 0 \\ \Delta/2 & -\Gamma_z & -\Gamma_t^* & 0 \\ 0 & -\Gamma_t & \Gamma_z & \Delta/2 \\ 0 & 0 & \Delta/2 & \xi_2 \end{pmatrix}, \tag{5}$$

where $\mathbf{\Gamma} = \mu_B \mathbf{B}$ and $\Gamma_t = \Gamma_x + i\Gamma_y$.

Simple formulas for the energy levels of the Hamiltonian (5) can be obtained in the limiting case $|\xi| \gg \eta, \Gamma$, where ξ and η are determined by the formulas $\xi_{1,2} = \xi \pm \eta/2$. I obtain

$$E_{1,2} = -\frac{v\Delta}{2u} \mp \left(\Gamma^2 u^4 - \Gamma_z \eta u^2 v^2 + \frac{\eta^2}{4} v^4 \right)^{1/2},$$

$$E_{3,4} = \frac{u\Delta}{2v} \mp \left(\Gamma^2 v^4 - \Gamma_z \eta u^2 v^2 + \frac{\eta^2}{4} u^4 \right)^{1/2}, \tag{6}$$

where $E_1 < E_2 < E_3 < E_4, u > 0, v > 0$,

$$u^2 = \frac{1}{2}\left(1 + \frac{\xi}{\sqrt{\Delta^2 + \xi^2}} \right), \quad v^2 = \frac{1}{2}\left(1 - \frac{\xi}{\sqrt{\Delta^2 + \xi^2}} \right).$$

The spontaneous magnetic moment of the ground state, $M_z = -\mu_B \partial E_1 / \partial \Gamma_z$, in the limit $\mathbf{\Gamma} \to 0$ is given by the expression:

$$M_z = -\mu_B \frac{\eta}{|\eta|} u^2.$$

Therefore the ground state is simultaneously superconducting and ferromagnetic.

Now let Δ be an internal effective field. The point is that in the region of a MQD the incoherent scattering of individual electronic quasiparticles of the contacts by the MQD, which leads to diffusional destruction of the superconducting phase, is negligibly small compared with the coherent proximity effect. The appearance of an effective field Δ increases the energy of the contacts (cf. Refs. 1 and 2), so that the ground-state energy of the system MQD + contacts is

$$E_1(\Delta) + \frac{1}{4\xi_0}\Delta^2, \tag{7}$$

where ξ_0 is a positive constant and $E_1(\Delta)$ is the ground-state energy (6). Minimizing expression (7) with respect to Δ and neglecting all small terms gives $\Delta = \sqrt{\xi_0^2 - \xi^2}$. The points $\xi = \pm\xi_0$ correspond to phase transitions into a state which is simultaneously superconducting and magnetic.

5. The limiting case $\xi_2 \gg \xi_1, \Gamma, \Delta$ corresponds to a small neighborhood of the critical point $\mu = \mu_{c1}$ of the phase transition I$\rightarrow$II and coexistence of the two phases I and II. The state $|1,1\rangle$, corresponding to phase III, is separated from the three other states by a large energy barrier. The effective Hamiltonian, which possesses transition matrix elements only between the three nearly degenerate states, can be obtained from Eq. (5) by crossing out the last row and column.

For small $\mathbf{\Gamma}$ the energies of the three states are ($E_1 < E_2 < E_3, \xi \equiv \xi_1$)

$$E_1 = \xi - \frac{\Delta u}{2v} - u^2\Gamma_z, \quad E_2 = \Gamma_z, \quad E_3 = \xi + \frac{\Delta v}{2u} - v^2\Gamma_z. \tag{8}$$

The spontaneous magnetic moment of the ground state in the limit $\mathbf{\Gamma} \rightarrow 0$ is $M_z = \mu_B u^2$.

If Δ is, as above, the internal magnetic field of the system MQD + contacts, its equilibrium value should be determined by minimizing expression (7) with $E_1(\Delta)$ from Eq. (8). For $\xi_c = \pm\xi_0 + \Gamma_z$ there exist phase transitions into a state which is simultaneously superconducting and magnetic.

In closing, it should be empahsized that an experimental check of Eqs. (6) and (8) for the energy spectrum of a MQD along with the formulas for the locations of the phase transition points would at the same time be an experimental check of the concept of superspace.

This work was a result of my visit to the Low-Temperature Laboratory at the Technical University of Helsinki. I thank M. Krusius and M. Paalanen for organizing the visit and for helpful discussions.

[1] A. F. Andreev, JETP Lett. **63**, 1018 (1996); **64**, 664 (1996).
[2] A. F. Andreev, Usp. Fiz. Nauk **168**, 655 (1998).
[3] D. C. Ralph, C. T. Black, and M. Tinkham, Phys. Rev. Lett. **74**, 3241 (1995); **76**, 688 (1996); **78**, 4087 (1997).
[4] G. C. Wick, A. S. Wightman, and E. P. Wigner, Phys. Rev. **88**, 101 (1952).
[5] M. T. Tuominen, J. M. Hergenrother, T. S. Tighe *et al.*, Phys. Rev. Lett. **69**, 1997 (1992).

Translated by M. E. Alferieff

Fractal structure of the phase equilibrium curve of a system of two oscillating magnetic moments

F. V. Lisovskiĭ[a)]
Institute of Radio Engineering and Electronics, Russian Academy of Sciences, 141120 Fryazino, Moscow Region, Russia

O. P. Polyakov
M. V. Lomonosov Moscow State University, 119899 Moscow, Russia

(Submitted 11 September 1998)
Pis'ma Zh. Éksp. Teor. Fiz. **68**, No. 8, 643–647 (25 October 1998)

The fractal structure of the phase equilibrium curve of a system of two interacting magnetic moments in the presence of a uniform low-frequency bias magnetic field is found by numerical methods. It is established that as frequency increases, the phase equilibrium curve becomes smooth. For that case an exact solution of the dynamical equations is found which gives a good description of the numerical results.
 [S0021-3640(98)01020-2]

PACS numbers: 05.45.+b, 75.60.Ej

It is now known reliably that dynamic self-organization of the distribution of the magnetization vector is possible in thin films of uniaxial magnets under the influence of a pulsating bipolar or monopolar bias magnetic field (see the original publications[1–4] and the reviews[5–8] and the bibliographies presented therein). The processes occurring here are either nonequilibrium phase transitions (PTs) of the type ''simple chaos'' → ''chiral chaos'' with formation of spiral domains[1–3,5,6] or PTs of the type ''simple chaos'' → ''order,'' in which the initial serpentine domain structure transforms into ordered biperiodic arrays with different motif-forming elements and different Bravais cells.[4,7,8] The theoretical analysis of phenomena of this kind encounters substantial difficulties in connection with the fact that the Landau–Lifshitz equation describing the evolution of the distribution $\mathbf{M}(\mathbf{r})$ of the magnetization vector in the general case does not have an analytical solution, even in the ''deterministic'' approach. For this reason, to determine the fundamental reasons for the appearance of self-organization in magnets it is necessary to simplify the corresponding theoretical models as much as possible.

We considered a system consisting of two point magnetic dipoles with moments $\mathbf{p}_1$ and $\mathbf{p}_2(|\mathbf{p}_1|=|\mathbf{p}_2|)$ located at the points $\mathbf{r}_1$ and $\mathbf{r}_2$, respectively, where $\mathbf{r}_1-\mathbf{r}_2=a\mathbf{e}_z$. It is known (see, for example, Ref. 9) that in the absence of external perturbations the ground state of such a system, which is twofold degenerate, corresponds to parallel orientation of the dipole moments, i.e., two configurations are possible: $\mathbf{p}_{1,2}=+p_{1,2}\mathbf{e}_z$ (state I) or $\mathbf{p}_{1,2}=-p_{1,2}\mathbf{e}_z$ (state II). The choice of one of the two possible configurations involves spontaneous symmetry breaking; in a real situation it is determined by the direction and

magnitude of the random or intentionally produced deviations of the dipole-moment vectors from the equilibrium state initially.

The temporal evolution of the dipole moment vectors $\mathbf{p}_{1,2}$, with allowance for the Gilbert dissipative term, is described by the equation[10]

$$\frac{d\mathbf{p}_{1,2}}{dt} = -\gamma\left[\mathbf{p}_{1,2}\frac{\delta w}{\delta \mathbf{p}_{1,2}}\right] + \frac{\alpha}{p_{1,2}}\left[\mathbf{p}_{1,2}\frac{\partial \mathbf{p}_{1,2}}{\partial t}\right], \tag{1}$$

where w is the total energy of the system, α is the damping parameter, and γ is the gyromagnetic ratio. For the model chosen, only the Zeeman and magnetostatic energies contribute to w, i.e.,

$$w = -(\mathbf{p}_1 \cdot \mathbf{H}_1) - (\mathbf{p}_2 \cdot \mathbf{H}_2), \tag{2}$$

where $\mathbf{H}_1 = \mathbf{H} + \mathbf{H}^{(21)}$, $\mathbf{H}_2 = \mathbf{H} + \mathbf{H}^{(12)}$, $\mathbf{H}$ is the intensity of the external magnetic field, and $\mathbf{H}_d^{(21)}(\mathbf{H}_d^{(12)})$ is the intensity of the dipole field produced by the second (first) magnetic moment at the first (second) magnetic moment.

For a harmonic external field $\mathbf{H} = \mathbf{e}_z H_0 \sin(\omega t)$ Eq. (1) reduces to the following system of equations for the spherical coordinates $\theta_{1,2}$ and $\phi_{1,2}$ of the vectors $\mathbf{p}_{1,2}$:

$$\frac{\partial \theta_{1,2}}{\partial \tau} = a_{p_{2,1}}[\sin(\phi_{1,2} - \phi_{2,1})] - \alpha a_H \sin\theta_{1,2} \sin\tau + \alpha a_{p_{2,1}}[-\alpha \sin\theta_{1,2}\cos\theta_{2,1} - \cos(\phi_{1,2} - \phi_{2,1})\cos\theta_{1,2}\sin\theta_{2,1}], \tag{3}$$

$$\frac{\partial \phi_{1,2}}{\partial \tau} = \frac{1}{\sin\theta_{1,2}}\{\alpha a_{p_{2,1}}[\sin(\phi_{1,2} - \phi_{2,1})]\sin\theta_{2,1} + a_H \sin\theta_{1,2}\sin\tau - a_{p_{2,1}} \times [-2\sin\theta_{1,2}\cos\theta_{2,1} - \cos(\phi_{1,2} - \phi_{2,1})\cos\theta_{1,2}\sin\theta_{2,1}]\}, \tag{4}$$

where $\tau = \omega t$, $a_{p_{1,2}}$, and a_H are dimensionless parameters defined by the expressions

$$a_{p_{1,2}} = \frac{\gamma p_{1,2}}{(1+\alpha^2)\omega a^3}, \quad a_H = \frac{\gamma H_0}{(1+\alpha^2)\omega}.$$

Analysis of Eqs. (3) and (4) leads to the following conclusions.

1. For any fixed values of the parameters $a_{p_{1,2}}$ and a_H the system evolves as $t \to \infty$ (depending on the initial conditions $\theta_{1,2}^{(0)} = \theta_{1,2}(t=0)$ and $\phi_{1,2}^{(0)} = \phi_{1,2}(t=0)$) to one of two possible equilibrium states with $\mathbf{p}_{1,2} = +p_{1,2}\mathbf{e}_z$ or $\mathbf{p}_{1,2} = -p_{1,2}\mathbf{e}_z$, i.e., there exist two attractors of the ''focus'' type.

2. If the Zeeman energy is much greater than the magnetostatic interaction energy of the dipoles ($a_H \gg a_{p_{1,2}}$), then Eq. (3) reduces to the form

$$\partial\theta_{1,2}/\partial\tau = -\alpha a_H \sin\theta_{1,2}\sin\tau$$

and has the analytical solution

$$\ln\left(\tan\frac{\theta_{1,2}}{2} \Big/ \tan\frac{\theta_{1,2}^{(0)}}{2}\right) = \alpha a_H(\cos\tau - 1). \tag{5}$$

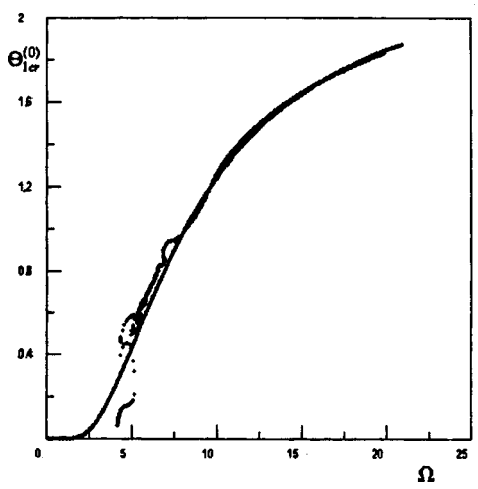

FIG. 1. Phase equilibrium curves for the nonequilibrium PT in the (Ω, θ_1) plane and $\alpha = 0.3$; $\theta_2^{(0)} = \pi/4$. Solid line — adiabatic approximation, dots — exact numerical solution of Eqs. (3) and (4) for $\phi_1^{(0)} = \phi_2^{(0)} = \pi/4$.

It follows from simple symmetry considerations that for the static case in the absence of an external magnetic field at the point of phase equilibrium between states I and II the angles θ_1 and θ_2 satisfy the relation

$$\theta_1 + \theta_2 = \pi,$$

and the magnetic moments of the dipoles are oriented parallel to $\mathbf{e}_z$ if $\theta_1 + \theta_2 < \pi$ and antiparallel to $\mathbf{e}_z$ if $\theta_1 + \theta_2 > \pi$.

If it is assumed that the same situation also occurs in the dynamic case, where the angles $\theta_{1,2}$ are functions of time, i.e., the adiabatic approximation is used, then it follows from Eqs. (5) that

$$\tan \frac{\theta_{1\mathrm{cr}}^{(0)}}{2} = \tan \frac{\pi - \theta_2^{(0)}}{2} \exp\left(- \frac{2\alpha}{\Omega} \right), \tag{6}$$

where $\Omega = 1/a_H$ is the dimensionless frequency of the external magnetic field and $\theta_{1\mathrm{cr}}^{(0)}$ is the critical value of the angle $\theta_1^{(0)}$ corresponding to the point of phase equilibrium for the chosen value of $\theta_2^{(0)}$ (as $t \to \infty$ for $\theta_1^{(0)} < \theta_{1\mathrm{cr}}^{(0)}$ the system passes into state I and for $\theta_1^{(0)} > \theta_{1\mathrm{cr}}^{(0)}$ it passes into state II).

The phase equilibrium curve for the nonequilibrium PT under study in the (Ω, θ_1) plane and for $\alpha = 0.3$ and $\theta_2^{(0)} = \pi/4$ is presented in Fig. 1. As $\Omega \to \infty$, $\theta_{1\mathrm{cr}}^{(0)}$ approaches $3\pi/4$ asymptotically (in complete agreement with the results obtained on the basis of the analogy with the static case). As the normalized frequency decreases, the critical value of $\theta_1^{(0)}$ decreases monotonically (formally — to zero at $\Omega = 0$), but it should be kept in mind that at low normalized frequencies (i.e., for large amplitudes of the ac magnetic field) the adiabatic approximation is inapplicable and the system of dynamical equations (3) and (4) must be solved exactly.

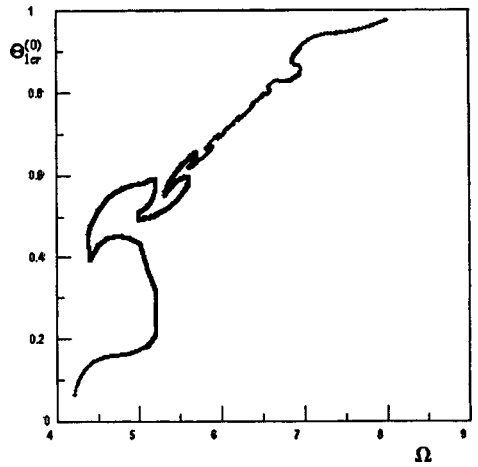

FIG. 2. A portion of the phase equilibrium curve (exact solution) shown in Fig. 1.

3. An exact numerical solution of Eqs. (3) and (4), for example, for the case $\alpha = 0.3$, $\theta_2^{(0)} = \pi/4$, and $\phi_1^{(0)} = \phi_2^{(0)}$, gives the phase equilibrium curve $\theta_{1\mathrm{cr}}^{(0)} = f(\Omega)$ constructed in Fig. 1 (dots); a portion of this curve is shown on a larger scale in Fig. 2. At high frequencies the exact solution gives results that are in good agreement with the predictions of the analytical theory based on the adiabatic approximation. At low frequencies the phase-equilibrium curve for the exact solution has a complex, irregular, fine structure and possesses a region of scaling and self-similarity that is characteristic for fractal objects.

4. We used the Hausdorff–Besicovitch method to determine the fractal dimension of the phase equilibrium curve.[11] The procedure used is illustrated in Fig. 3, which shows

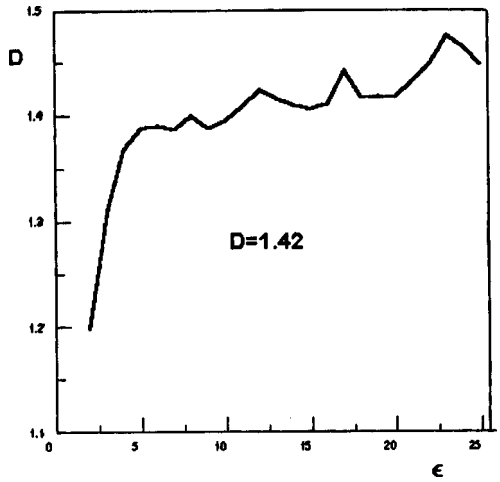

FIG. 3. Fractal dimension D versus the edge length ε of a hypercube for the phase equilibrium curve shown in Figs. 1 and 2 (exact solution).

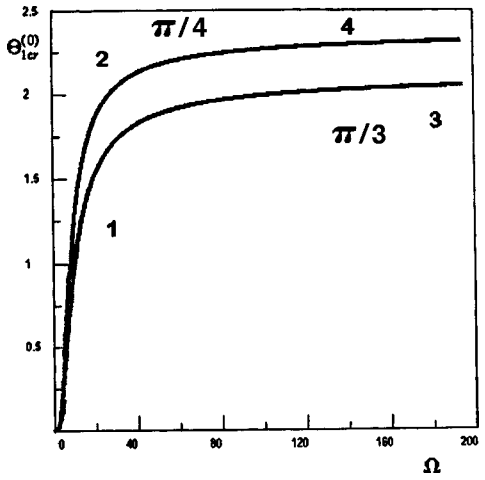

FIG. 4. Phase equilibrium curves in the (Ω, θ_1) plane that correspond to the exact numerical solution of Eqs. (3) and (4) and the adiabatic approximation for $\alpha = 0.3$, $\phi_1^{(0)} = \phi_2^{(0)} = \pi/4$; *1,3* — $\theta_2^{(0)} = \pi/3$, *2,4* — $\theta_2^{(0)} = \pi/4$.

the fractal dimension D as a function of the edge length ε of a hypercube. It is obvious that the phase equilibrium curve at low frequencies does indeed exhibit scaling, and its fractal dimension is $D = 1.42$.

5. The behavior described above for the dynamical system under study is also observed with other initial conditions. As an example, Fig. 4 shows phase equilibrium curves for $\alpha = 0.3$, $\theta_2^{(0)} = \pi/3$, $\phi_1^{(0)} = \phi_2^{(0)} = \pi/4$ (*1* — exact solution, *3* — adiabatic approximation) for a wide range of values of the normalized frequency Ω. For convenience in making comparisons, the figure also displays similar curves (*2* — exact solution, *4* — adiabatic approximation) for $\theta_2^{(0)} = \pi/4$, to which Figs. 1 and 2 refer.

The investigations performed show that our simple model of a magnetic system with lumped parameters exhibits many features that are characteristic for complex open nonequilibrium distributed systems. Specifically, the experimentally observed[6,7] character of the nonequilibrium phase transitions from one synergetic structure to another exhibits a qualitative analogy with the behavior of the model studied (appearance of ordering and fractal-like structures at low external-field frequency, the vanishing of these structures as the frequency increases, high sensitivity to changes in any parameter of the system or external field, and so on). All this attests to the general nature of the dynamic self-organization in different open nonequilibrium systems.

In conclusion, we note that the physicists have long recognized that the formalism of fractal geometry must be used in order to give an adequate description of phenomena accompanying equilibrium and nonequilibrium PTs. A classic example is the hypothesis of the fractal nature of the critical state. This hypothesis is the basis of the renormalization-group method. Dikshteĭn *et al.*[12] recently called attention to the appearance of static fractal-like domain walls in thin uniaxial magnetic films as film thickness increases above a certain critical value. In our example, however, we encounter a fundamentally new phenomenon — the possibility of fractalization of phase equilibrium curves.

We thank L. I. Antonov for a discussion of this work and for helpful suggestions.

This work was supported by the Russian Fund for Fundamental Research (Project No. 96-02-16082-a).

[a)]e-mail: lisf@dataforce.net

[1] G. S. Kandaurova and A. É. Sviderskiĭ, JETP Lett. **47**, 490 (1988).
[2] G. S. Kandaurova, Dokl. Akad. Nauk SSSR **308**, 1364 (1989) [Sov. Phys. Dokl. **34**, 918 (1989)].
[3] F. V. Lisovskiĭ and E. G. Mansvetova, Fiz. Tverd. Tela (Leningrad) **31**, 273 (1989) [Sov. Phys. Solid State **31**, 876 (1992)].
[4] F. V. Lisovskiĭ and E. G. Mansvetova, JETP Lett. **55**, 32 (1992).
[5] G. S. Kandaurova and A. É. Sviderskiĭ, Zh. Éksp. Teor. Fiz. **97**, 1218 (1990) [Sov. Phys. JETP **70**, 684 (1991)].
[6] I. E. Dikshteĭn, F. V. Lisovskiĭ, and E. G. Mansvetova, Zh. Éksp. Teor. Fiz. **100**, 1606 (1991) [Sov. Phys. JETP **73**, 888 (1991)].
[7] F. V. Lisovskiĭ, E. G. Mansvetova, E. P. Nikolaeva, and A. V. Nikolaev, Zh. Éksp. Teor. Fiz. **103**, 213 (1993) [JETP **76**, 117 (1993)].
[8] F. V. Lisovskiĭ, E. G. Mansvetova, and Ch. M. Pak, Zh. Éksp. Teor. Fiz. **108**, 1031 (1995) [JETP **81**, 567 (1995)].
[9] L. I. Antonov, L. G. Dedenko, and A. N. Matveev, *Methods for Solving Electricity Problems*, Nauka, Moscow, 1982.
[10] S. V. Vonsovskiĭ, *Magnetism*, Nauka, Moscow, 1971.
[11] Pierre Berge, Yves Pomeau, and Christian Vidal, *L'Ordre dans le Chaos*, Hermann, Editeurs des Sciences et des Arts [Mir, Moscow, 1991].
[12] I. E. Dikshteĭn, D. V. Kuznetsov, F. V. Lisovskiĭ *et al.*, in *Abstracts of the 16th International School-Seminar on New Magnetic Materials for Micorelectronics* [in Russian], Moscow State University, Moscow, 1998, p. 519.

Translated by M. E. Alferieff